AGU PUBLICATIONS

JGR

Journal of Geophysical Research: Space Physics

RESEARCH ARTICLE

10.1002/2014JA020778

Key Points:
- New technique to search for a subsurface ocean in Ganymede with a telescope
- Ocean affects auroral oscillation caused by time-varying external magnetic field
- HST observations reveal weak auroral oscillation and imply existence of ocean

Correspondence to:
J. Saur,
saur@geo.uni-koeln.de

Citation:
Saur, J., et al. (2015), The search for a subsurface ocean in Ganymede with Hubble Space Telescope observations of its auroral ovals, *J. Geophys. Res. Space Physics*, *120*, 1715–1737, doi:10.1002/2014JA020778.

Received 4 NOV 2014
Accepted 28 JAN 2015
Accepted article online 3 FEB 2015
Published online 12 MAR 2015

The search for a subsurface ocean in Ganymede with Hubble Space Telescope observations of its auroral ovals

Joachim Saur[1], Stefan Duling[1], Lorenz Roth[2,3], Xianzhe Jia[4], Darrell F. Strobel[5,6], Paul D. Feldman[6], Ulrich R. Christensen[7], Kurt D. Retherford[2], Melissa A. McGrath[8], Fabrizio Musacchio[1], Alexandre Wennmacher[1], Fritz M. Neubauer[1], Sven Simon[9], and Oliver Hartkorn[1]

[1]Institute of Geophysics and Meteorology, University of Cologne, Cologne, Germany, [2]Southwest Research Institute, San Antonio, Texas, USA, [3]School of Electrical Engineering, Royal Institute of Technology, Stockholm, Sweden, [4]Department of Atmospheric, Oceanic, and Space Sciences, University of Michigan, Ann Arbor, Michigan, USA, [5]Department of Earth and Planetary Sciences, Johns Hopkins University, Baltimore, Maryland, USA, [6]Department of Physics and Astronomy, Johns Hopkins University, Baltimore, Maryland, USA, [7]Max Planck Institute for Solar System Research, Göttingen, Germany, [8]Marshall Space Flight Center, Huntsville, Alabama, USA, [9]School of Earth and Atmospheric Sciences, Georgia Institute of Technology, Atlanta, Georgia, USA

Abstract We present a new approach to search for a subsurface ocean within Ganymede through observations and modeling of the dynamics of its auroral ovals. The locations of the auroral ovals oscillate due to Jupiter's time-varying magnetospheric field seen in the rest frame of Ganymede. If an electrically conductive ocean is present, the external time-varying magnetic field is reduced due to induction within the ocean and the oscillation amplitude of the ovals decreases. Hubble Space Telescope (HST) observations show that the locations of the ovals oscillate on average by 2.0° ± 1.3°. Our model calculations predict a significantly stronger oscillation by 5.8° ± 1.3° without ocean compared to 2.2° ± 1.3° if an ocean is present. Because the ocean and the no-ocean hypotheses cannot be separated by simple visual inspection of individual HST images, we apply a statistical analysis including a Monte Carlo test to also address the uncertainty caused by the patchiness of observed emissions. The observations require a minimum electrical conductivity of 0.09 S/m for an ocean assumed to be located between 150 km and 250 km depth or alternatively a maximum depth of the top of the ocean at 330 km. Our analysis implies that Ganymede's dynamo possesses an outstandingly low quadrupole-to-dipole moment ratio. The new technique applied here is suited to probe the interior of other planetary bodies by monitoring their auroral response to time-varying magnetic fields.

1. Introduction

Jupiter's moon Ganymede, the largest satellite in our solar system, is a fully differentiated body and the only known satellite with an internal dynamo field [*Kivelson et al.*, 1996]. It possesses an iron core, the source region of the dynamo, a silicate mantle, and an ice mantle as the outer layer [*Anderson et al.*, 1996]. Magnetic field measurements taken by the Galileo spacecraft suggest the existence of a layer of liquid water sandwiched between an ice shell at the surface and a deep layer of a high-pressure polymorph of ice, but these interpretations of the magnetometer data are not conclusive [*Kivelson et al.*, 2002] as we detail further below.

Ganymede also exhibits auroral emission, first observed by *Hall et al.* [1998] with the Goddard High Resolution Spectrograph (GHRS) on board of the Hubble Space Telescope (HST). These observations constrained the fluxes and spectral shapes of the OI 1356 Å and OI 1304 Å emission lines, which imply a molecular oxygen atmosphere with a column density in the range of (1–10) × 10^{14} cm^{-2} [*Hall et al.*, 1998]. The line shape of the OI 1356 Å emission is consistent with the radiation being emitted from two circumpolar auroral ovals situated in the north and south polar regions of Ganymede. Subsequent spatially and spectrally resolved HST observations with the Space Telescope Imaging Spectrograph (STIS) clearly demonstrate the existence of two auroral ovals around Ganymede's magnetic north and south poles as shown in the work of *Feldman et al.* [2000] and *McGrath et al.* [2013]. In the latter work four sets of HST observations of Ganymede's UV aurora acquired during a time span from 1998 to 2007 are used to analyze the time-averaged locations of Ganymede's auroral ovals. *McGrath et al.* [2013] show that the auroral ovals are located at high latitudes on the upstream (i.e., orbital trailing) hemisphere of Ganymede and much closer

©2015. American Geophysical Union. All Rights Reserved.

to Ganymede's equator on the downstream (i.e., orbital leading) hemisphere. Due to the relative strength of Ganymede's internal dynamo field (~750 nT at the equator) and Jupiter's magnetospheric field at the orbital distance of Ganymede (~100 nT), Ganymede possesses a closed field line region above its surface and a mini-magnetosphere within Jupiter's giant magnetosphere. The magnetosphere of Ganymede is unique in the solar system as it is sub-Alfvénic, and thus, no bow shock forms upstream of Ganymede, but Alfvén wings connecting Ganymede to Jupiter's ionosphere are generated (for further discussion, see, e.g., *Kivelson et al.* [1998] and *Neubauer* [1998]). The upstream-downstream emission pattern and asymmetries reported in *McGrath et al.* [2013] are strongly governed by this sub-Alfvénic interaction of Jupiter's magnetospheric plasma with Ganymede's mini-magnetosphere [*Neubauer*, 1998; *Jia et al.*, 2009]. In contrast to Ganymede's sub-Alfvénic interaction, the interaction of the Earth's magnetosphere with the solar wind plasma is only very exceptionally sub-Alfvénic [*Chané et al.*, 2012]. Ganymede, as a magnetized planetary body embedded in a sub-Alfvénic plasma flow, is considered a textbook example of the expected plasma environment around close-in extrasolar planets [e.g., *Ip et al.*, 2004; *Saur et al.*, 2013]. Extrasolar planets at radial distances of less than approximately 0.1 AU are typically estimated to be exposed to stellar winds with sub-Alfvénic velocities [*Saur et al.*, 2013]. Even though intrinsic magnetic fields of extrasolar planets have not yet been directly observed, they have been indirectly inferred [*Kislyakova et al.*, 2014] and are generally expected to be present [*Christensen et al.*, 2009].

The locations of the auroral ovals, similar to any other aurorae in our solar system, are strongly controlled by the magnetic field environment around the planetary body. Determining the locations of the auroral ovals thus provides constraints on the magnetic field environment. Ganymede's magnetic field environment is complex. It consists of internal contributions from Ganymede's deeply rooted dynamo magnetic field and possibly due to electrodynamic induction if a saline subsurface ocean is present [e.g., *Kivelson et al.*, 2002; *Seufert et al.*, 2011]. Additionally, there are external contributions due to Jupiter's magnetospheric field at the location of Ganymede and due to the plasma interaction of Ganymede with the plasma of Jupiter's magnetosphere [*Neubauer*, 1998; *Jia et al.*, 2009]. The magnetic field environment of Ganymede has been probed with in situ magnetometer measurements [*Kivelson et al.*, 1996, 1998; *Volwerk et al.*, 1999; *Kivelson et al.*, 2002] and studied with numerical simulations on various levels of detail [*Kopp and Ip*, 2002; *Ip and Kopp*, 2002; *Paty and Winglee*, 2004, 2006; *Paty et al.*, 2008; *Jia et al.*, 2008, 2009; *Jia et al.*, 2010; *Duling et al.*, 2014].

As demonstrated by *Eviatar et al.* [2001], the electrons of Jupiter's magnetosphere do not have sufficient energy to excite the auroral emissions, in contrast to the aurorae generated at Io and Europa [e.g., *Saur et al.*, 1998, 2000; *Retherford et al.*, 2000; *Roth et al.*, 2011, 2014]. At Ganymede, local particle acceleration is necessary to explain the observed UV fluxes. According to *Eviatar et al.* [2001], the two possible energization mechanisms include stochastic acceleration by collective plasma effects and acceleration by electric fields associated with field-aligned Birkeland currents. Despite this work, it needs to be noted that due to the lack of systematic observations and associated studies, the kinetic processes leading to Ganymede's aurora are generally considered as not completely understood.

A key question about Ganymede is whether it possesses a subsurface water ocean under its icy crust. Even though several theoretical models of Ganymede's interior suggest the possibility of a subsurface ocean [e.g., *Sohl et al.*, 2002; *Hussmann et al.*, 2006; *Rambaux et al.*, 2011; *Vance et al.*, 2014], the so far only observational evidence for the existence of a subsurface ocean comes from magnetic field measurements by the Galileo spacecraft taken during several Ganymede flybys [*Kivelson et al.*, 2002]. The time-variable magnetic field of Jupiter's magnetosphere seen in the rest frame of Ganymede is periodically changing with Jupiter's synodic rotation period of 10.5 h. This time-variable magnetic field component will induce secondary magnetic fields within an electrically conductive subsurface ocean. The radial component of Jupiter's magnetospheric field is the dominant time-variable component and changes from toward (+80 nT) to away from Jupiter (−80 nT) with Jupiter's synodic rotation [*Kivelson et al.*, 2002; *Seufert et al.*, 2011]. The time-averaged magnitude of Jupiter's magnetospheric field at the radial distance of Ganymede's orbit is around 100 nT [*Kivelson et al.*, 2004]. The variability of the radial component dominates the variability of the azimuthal component due to the current sheet effects in Jupiter's magnetosphere [*Kivelson et al.*, 2002; *Seufert et al.*, 2011].

The magnetic field measurements near Ganymede reported by *Kivelson et al.* [2002] are equally consistent with two models for Ganymede's internal magnetic field contributions: A dynamo dipole field plus

©2015. American Geophysical Union. All Rights Reserved.

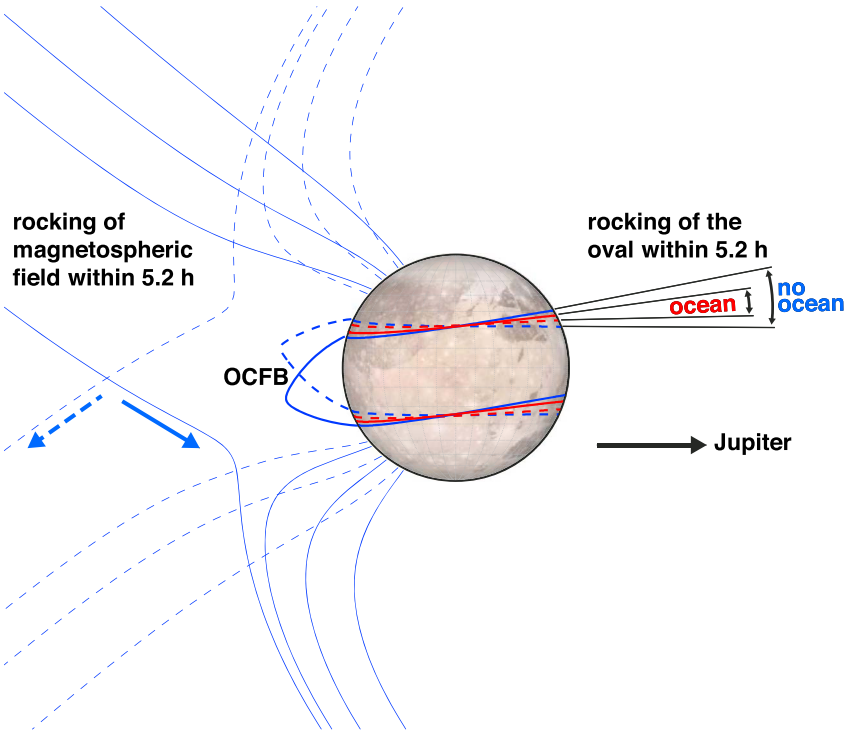

Figure 1. Sketch of selected magnetic field lines and locations of auroral ovals when Ganymede is above (dashed lines) and below the current sheet (solid lines), respectively. The ovals are located where the open-closed field line boundary (OCFB) intersects Ganymede's surface. Induction in an ocean partly compensates Jupiter's time-variable field and thus reduces the oscillation of the ovals (red: with ocean; blue: without ocean). The magnetic field environment in this sketch has been simplified for clarity by including internal dipole moments, the time-variable external field, induction in an ocean, and as proxy for the plasma magnetic field a constant field contribution within the OCFB generated by surface currents on the OCFB.

quadrupole moments (whose contributions are small but necessary for the fit to the Galileo magnetometer data) or a dynamo dipole field plus a field induced by the locally time-variable component of Jupiter's magnetic field within a saline, electrically conductive subsurface ocean. The basic reason for this ambiguity is that with measurements acquired during single flybys, which do not occur on exactly the same trajectory, it is impossible to distinguish between spatial variations (i.e., higher order moments) and temporal variations (i.e., induction). *Kivelson et al.* [2002] gave preference to the model with an induced field, because it allowed to fit the observations with fewer free parameters than in the model with an internal quadrupole. However, we note that only two of the five quadrupole coefficients turned out to make a significant contribution. Although there is no obvious a priori reason for neglecting the others, in principle it is possible to fit the measurements with a similar number of free parameters as in the model with an induced field. The evidence for the existence of an ocean, based on the magnetometer data alone, is therefore inconclusive.

The idea of this work is to search for an ocean within Ganymede by monitoring the time variability of the locations of the auroral ovals. Based on numerical modeling we demonstrate how an electrically conductive subsurface ocean affects the variability of the locations of Ganymede's auroral ovals in response to the time-variable magnetic field of Jupiter's magnetosphere seen in the rest frame of Ganymede. Ganymede's auroral ovals are expected to be located where the open-closed field line boundary of its mini-magnetosphere intersects with Ganymede's surface [*Eviatar et al.*, 2000, 2001; *Jia et al.*, 2009, 2010; *McGrath et al.*, 2013]. The open-closed field line boundary is the area/surface that separates magnetic field lines starting and ending on Ganymede from field lines connecting to Jupiter. Because the locations of the auroral ovals are controlled by the magnetic field environment, we expect the auroral ovals to change their locations, i.e., to oscillate up and down in concert with the radial component of Jupiter's magnetospheric field. The resultant locations of the ovals are sketched as blue lines in Figure 1. When a saline, electrically conductive subsurface ocean is present, the time-variable magnetic field component will be compensated

©2015. American Geophysical Union. All Rights Reserved.

Table 1. Exposure Details of HST Campaign ID 12244[a]

Visit #	Orbit #	Exp #	Date UTC	Start UTC	Exp Time (s)	Sub Obs Long (°)	Sub Obs Lat (°)	Sys III Long (°)	Magnet Lat (°)	Used
1	1	1	2010-11-19	20:11:18	798.182	97.7	1.92	176.9	8.68	1
1	1	2	2010-11-19	20:28:04	798.196	98.3	1.92	186.4	9.20	1
1	2	3	2010-11-19	21:25:54	1179.197	100.4	1.92	221.2	8.90	1
1	2	4	2010-11-19	21:52:46	1179.191	101.4	1.92	236.5	7.72	1
1	3	5	2010-11-19	23:01:45	1179.198	103.8	1.92	275.8	2.46	0
1	3	6	2010-11-19	23:28:37	1179.197	104.7	1.92	291.1	−0.05	0
1	4	7	2010-11-20	00:37:37	1179.199	107.1	1.92	330.4	−6.06	0
1	4	8	2010-11-20	01:04:29	1179.192	108.1	1.92	345.7	−7.77	1
1	5	9	2010-11-20	02:13:28	1179.199	110.5	1.92	25.0	−9.47	1
1	5	10	2010-11-20	02:40:20	1179.198	111.4	1.92	40.3	−8.95	1
2	1	1	2011-10-01	09:38:24	813.190	90.8	3.38	167.5	7.95	1
2	1	2	2011-10-01	09:55:25	813.200	91.4	3.38	177.2	8.71	1
2	2	3	2011-10-01	10:55:46	1194.198	93.7	3.38	213.4	9.27	1
2	2	4	2011-10-01	11:22:53	1194.199	94.6	3.38	228.9	8.38	1
2	3	5	2011-10-01	12:47:53	813.196	97.5	3.38	275.5	2.51	0
2	3	6	2011-10-01	13:04:54	813.198	98.1	3.38	285.2	0.93	0
2	4	7	2011-10-01	14:07:24	1194.196	100.4	3.38	332.6	−5.01	0
2	4	8	2011-10-01	14:34:31	1194.198	101.3	3.38	338.1	−6.98	1
2	5	9	2011-10-01	15:43:53	1209.195	103.8	3.38	17.6	−9.49	1
2	5	10	2011-10-01	16:07:30	1209.195	104.6	3.38	31.1	−9.35	1

[a]The columns from left to right provide visit, orbit, and exposure numbers, respectively, start time and duration of each exposure, subobserver longitude and latitude, system III longitude and magnetic latitude, and a qualifier if the observations are used for measuring the rocking of the ovals.

by fields induced due to Faraday's law of induction within the ocean. Thus, the time-variable external field component as well as the amplitude of the oscillation of the ovals decrease as shown as red lines in Figure 1.

In order to observationally constrain the amplitudes of the oscillations of the ovals, we analyze time-dependent spatially resolved HST observations, which we particularly designed and scheduled to search for a subsurface ocean. The two-dimensional and explicitly time-dependent nature of the HST observations enable us to separate spatial and temporal variations. They are therefore not subject to the ambiguity of the in situ magnetic field observations of single flybys [*Kivelson et al.*, 2002]. We combine these observations with three-dimensional MHD modeling for a quantitative analysis of the auroral responses. We note that observations of auroral phenomena have been used in the past to constrain planetary magnetic fields. For example, *Connerney et al.* [1998] and *Hess et al.* [2011] used observations of the Io's auroral footprint to derive an improved model of Jupiter's magnetic field.

The remainder of this work is structured as follows: In section 2 we introduce the two sets of HST data used in our analysis and explain how the data are processed. We also describe how the amplitudes of the oscillations of ovals are extracted from the data. In section 3 we introduce the magnetohydrodynamic (MHD) models developed by *Duling et al.* [2014], which we use to both demonstrate the effects of an ocean on the auroral responses in general and to quantitatively interpret the HST observations. The results of the observations are presented in section 4. Using the independent MHD model from *Jia et al.* [2009], we also present a detailed study of the robustness of the modeled differences of the auroral locations with and without ocean. We also discuss constraints and implications for the subsurface ocean and Ganymede's dynamo magnetic field. In section 5 we summarize and discuss our results. In Appendix A we investigate the effects of possible ways to process and analyze the data (such as, e.g., smoothing). In Appendix B we introduce a formal procedure to estimate the errors of the amplitudes of the auroral oscillations, and in Appendix C we present a Monte Carlo test as a more realistic means to estimate these uncertainties.

2. Observations and Data Processing

In this section we describe the observations, the raw data processing, and how we extract the amplitude of the oscillations of the ovals from the data.

©2015. American Geophysical Union. All Rights Reserved.

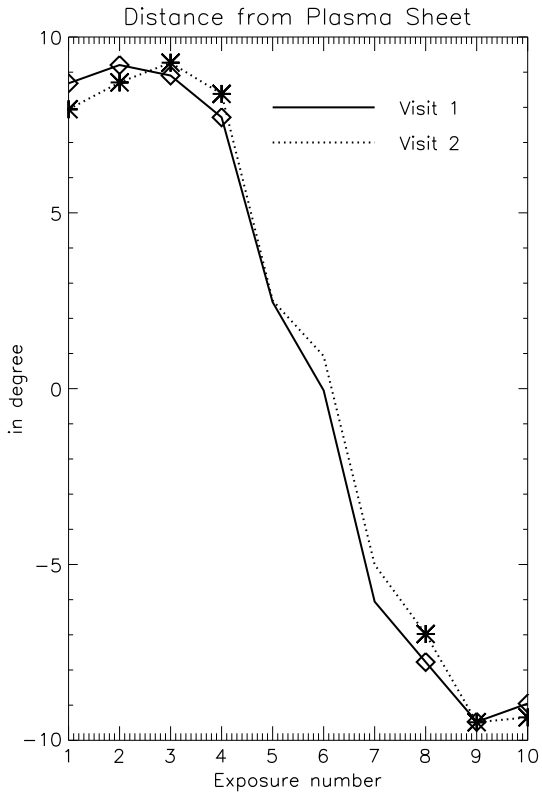

Figure 2. Distance from plasma sheet, i.e., magnetic Jovian latitude for both HST visits as a function of exposure number. Marked exposures are used for the measuring of the rocking angle α (see also Table 1).

2.1. Scheduling Information and Raw Data Processing

In this work we analyze observations acquired during HST campaign ID 12244, where two visits with five consecutive HST orbits each were dedicated to observing Ganymede at eastern elongation. Thus, HST observed Ganymede's orbitally leading hemisphere, which is the downstream hemisphere with respect to the unperturbed flow of magnetospheric plasma past Ganymede. Visit 1 occurred on 19 November 2010, and visit 2 occurred on 1 October 2011. Details of both visits are summarized in Table 1. With durations of approximately 7 h each, both visits cover more than half of Jupiter's synodic rotation period. The time windows of both visits were designed such that the Jovian magnetic latitudes of Ganymede span the entire possible range, i.e., Ganymede is exposed to the maximum variability of Jupiter's magnetospheric field during each visit. Figure 2 shows that Ganymede's magnetic latitude coverage was very similar for both visits. The magnetic latitudes Θ_M are calculated according to $\Theta_M = 9.5° \cos(\lambda_{III} - 200.8°)$, where λ_{III} describes the system III longitude of Ganymede [*Dessler*, 1983; *Connerney et al.*, 1998]. When Ganymede is at maximum positive latitude, the radial component of Jupiter's magnetospheric field B_r assumes its positive maximum. When Ganymede is at maximum negative latitude, B_r assumes its negative maximum. For the analysis of the rocking of the aurora we use exposures where Ganymede is located near-maximum magnetic latitudes, i.e., $|\Theta_M| \gtrsim 7°$, to measure the maximum amplitude of the oscillation of the auroral ovals. The resultant exposures are marked in Table 1 and in Figure 2 with diamonds and crosses.

The observations were performed with the Space Telescope Imaging Spectrograph (*HST/STIS*) using grating G140L and pseudo aperture 52x2D1. This aperture relocates the position of Ganymede's spectral image away from the region where the Multi-Anode Micro-channel Array (MAMA) detector suffers from large dark currents (i.e., away from the "blotch"). We find the location of the disk of Ganymede on the detector by convolving the Lyman α emission with a theoretical disk of the same size as Ganymede. We assumed that the theoretical disk is uniform due to the lack of appropriate Lyman α maps of Ganymede. The location of the theoretical disk where the integrated convolved flux attains the maximum corresponds to the center of the Lyman α disk. We also use the long-wavelength trace of the image to independently confirm the vertical location of the disk of Ganymede. The dispersion is predominantly in the horizontal direction on the detector. However, the spectral trace slightly shifts in vertical direction on the detector as a function of its horizontal position in the flat fielded raw data, which we use in this analysis. Here we refer to the vertical direction as the direction parallel to the slit. The horizontal direction is perpendicular to the slit and approximately along the direction of dispersion. We use calibration measurements of the stellar object WD2126+734 to determine the vertical drift of the dispersion when the pseudo aperture 52x2D1 is used in combination with G140L (PI: C. Proffitt, ID: 10040, filename: o8tg02020_flt.fits). In this analysis we investigate the spatial and temporal structure of the oxygen OI 1356 Å emissions due to their superior brightness and low component of solar reflected light compared to other atmospheric emission lines at FUV wavelengths. For comparison, the total averaged flux from Ganymede's atmosphere at 1304 Å is on average weaker by a factor of 1.8 than the fluxes at 1356 Å [*Feldman et al.*, 2000]. About half of the emission at 1304 Å is due to solar radiation reflected from the surface. The solar flux at 1356 Å is less than 10% that of the 1304 Å

©2015. American Geophysical Union. All Rights Reserved.

multiplet, and thus, reflected light contributes only very weakly to the observed emission at 1356 Å. The 1304 Å emission additionally has contributions due to solar resonant scattering, which is negligible for the 1356 Å emission [*Hall et al.*, 1998; *Feldman et al.*, 2000]. For these reasons only the 1356 Å emission is used in this work. The resultant location of the center of the 1356 Å disk calculated from the location of the Lyman α disk and the long-wavelength trace is given by detector pixel i_x = 404 and i_y = 102 for both visits, i.e., in horizontal and vertical direction, respectively.

For a quantitive analysis of the observed auroral fluxes, we first remove the background emission due to dark noise and other sources. For this purpose we average the fluxes in rows above and below the OI 1356 Å image to determine the background fluxes and then remove this flux from the OI 1356 Å image. We use solar spectra measured by the Solar Extreme-Ultraviolet Experiment (SEE) on the Thermosphere Ionosphere Mesosphere Energetics and Dynamics (TIMED) mission [*Woods et al.*, 2005] for the particular days of the observations in order to model the solar reflected light from the surface of Ganymede. For determining the albedo, the long-wavelength image of the observations (λ = 1413 Å to 1586 Å) is used. We find a geometric albedo of 0.017 ± 0.003 for visit 1 and 0.019 ± 0.003 for visit 2 on the leading side. The albedo values of this study are similar to values for the albedo on the trailing side of 0.023 ± 0.002 derived from fluxes near 1400 Å by *Feldman et al.* [2000] from HST/STIS observations and an albedo of 0.026 ± 0.003 derived by *Hall et al.* [1998] from *HST/GHRS* measurements of the reflected C II 1335 Å multiplet. Due to a lack of knowledge of the spatial structure of the FUV albedo, we assumed similar to previous studies that the albedo is spatially constant. We note that modifications of the albedo values have a negligible effect on the derived rocking angles of this analysis.

The modeled reflected flux is then convolved with the point spread function (PSF), which we obtained with the *TinyTim* simulation software package from the website `tinytim.stsci.edu` [*Krist et al.*, 2011]. The PSF has a Gaussian structure near the central pixel and power law wings at larger distances from the central pixel similar to the kappa-PSF(κ, γ) [*Saur et al.*, 2011], which is identical to a Lorentzian profile for $\kappa = \gamma = 2$. The fluxes of the reflected light are then finally removed from the observed OI 1356 Å flux, and the images are rotated with Jupiter's north pointing upward. The direction from south to north will also be referred to as the *y* direction. The *x* direction is perpendicular to it, which is approximately toward Jupiter. After these data processing steps the remaining fluxes are purely due to emission from Ganymede's atmosphere aside from statistical noise.

The resultant images are grainy, i.e., the pixel brightness is somewhat erratic due to the Poisson distributed fluxes. This effect can be reduced by a smoothing filter. We use a filter of the form

$$f_s(i_x, i_y) = \frac{1}{8}\left(4f(i_x, i_y) + f(i_x - 1, i_y) + f(i_x + 1, i_y) + f(i_x, i_y - 1) + f(i_x, i_y + 1)\right) \quad (1)$$

applied 4 times. The filter is referred to as star filter with i_x and i_y referring to pixel coordinates in the rotated images. The effects of the star filter in comparison with other filter applications are discussed in Appendix A.

The resultant images for visit 1 where all exposures are superposed when Ganymede was at sufficiently large latitudes above the current sheet ($\Theta_M \gtrsim 7°$) and below the current sheet ($\Theta_M \lesssim -7°$) are shown in Figure 3, respectively. Similar images are shown for the second visit taken roughly one year later in Figure 4.

The apparent emissions above the right limb stem from the weaker emission line (OI 1358.5 Å) of the observed oxygen doublet, whose position is shifted by 5 pixels to the right and up in the rotated images. Since we only use pixels with brightness of 80% and more of the brightest pixels along the ovals, the effect on identifying the auroral ovals is expected to be small.

The pixel size on the *STIS* FUV-MAMA detector corresponds to 0.0246 arcsec. The spectral resolution (full width at half maximum) for a point source at 1500 Å is 1.5 pixels for all slits [*Hernandez et al.*, 2014]. We use the 2 arcsec slit to obtain spectral images of Ganymede. Ganymede subtends ~1.75 arcsec in diameter at the time of observations which corresponds to ~70 pixels, but only 70/1.5 = 47 resolution elements across on a monochromatic image at 1500 Å assuming monochromatic lines. One pixel corresponds to approximately 0.03 R_G (with the Ganymede radius R_G = 2631 km). For Nyquist sampling, we have 70/2 = 35 resolution elements, which corresponds to a spatial resolution of 0.05 arcsec. The resolution of 0.05 arcsec is less than the average width of the oval of 0.18 R_G, which corresponds to 0.16 arcsec or 6.5 pixels. Thus, the ovals are resolved approximately by a factor (0.16 arcsec)/(0.05 arcsec) = 3.2. Note that the applied smoothing procedure broadens the auroral ovals by approximately 1.5 pixels.

©2015. American Geophysical Union. All Rights Reserved.

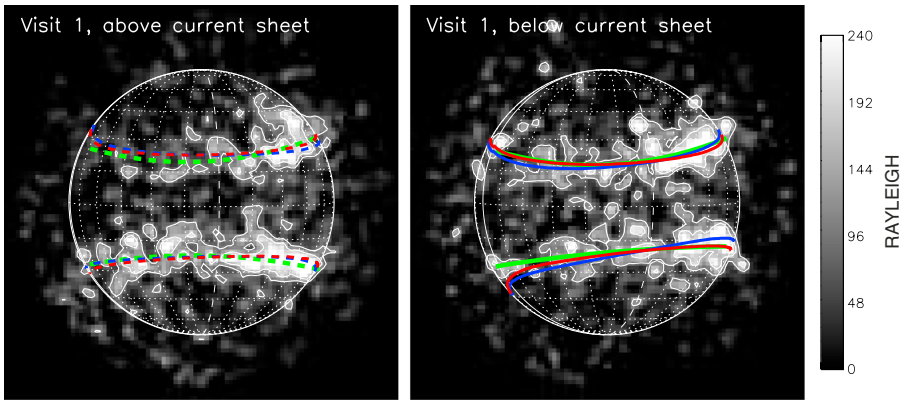

Figure 3. Visit 1: Observed auroral brightness in Rayleigh at OI 1356 Å when Ganymede is (left) above and (right) below the current sheet. Contours are for 110 and 170 Rayleigh. North is up and Jupiter to the right. Green lines display fits to the observation, red and blue lines display model locations with and without ocean, respectively.

2.2. Location of the Ovals

The location of the ovals for each column, i.e., for each i_x, is determined by

$$y(i_x) = \frac{\sum_{i_y} i_y (f(i_x, i_y) - f_{\min}(i_x))}{\sum_{i_y} (f(i_x, i_y) - f_{\min}(i_x))}, \tag{2}$$

where the summation is over all i_y for which $f(i_x, i_y) > f_{\min}(i_x)$. The minimum is chosen such that $f_{\min}(i_x)$ corresponds to 80% of the brightest pixel in each column i_x. The brightest pixels are searched in each hemisphere within 5° and 60° north and within 5° and 60° south consistent with oval locations from previous observations [*McGrath et al.*, 2013]. The method to define the locations of the ovals in (2) considers the fluxes in the y direction exceeding a cutoff level of 80% of the brightest pixel (in each column i_x, respectively). The method thus considers the emissions in the vicinity of the peak emissions of the ovals, but it discards the effects of other atmospheric UV emissions from Ganymede, i.e., polar excited emissions due to energetic electrons in Jupiter's magnetosphere or equatorial emissions excited from energetic electrons within Ganymede's mini-magnetosphere. The 80% value for the cutoff was deliberately chosen relatively high to clearly separate the emission from the oval compared to other more polar and equatorial emissions. Due to the brightness variation in x direction of the ovals, we choose $f_{\min}(x)$ to vary in x direction. We also investigated other methods to determine the locations of the ovals, which are described and compared against each other in Appendix A.

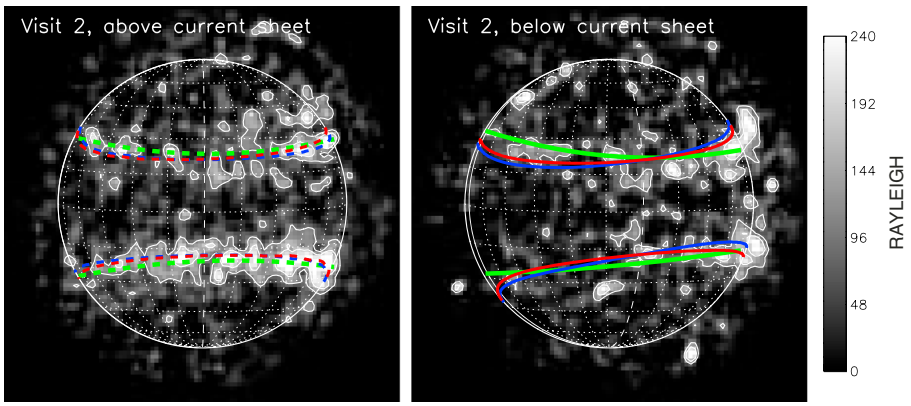

Figure 4. Visit 2: Observed auroral brightness in Rayleigh at OI 1356 Å when Ganymede is (left) above and (right) below the current sheet. Other properties are similar as in Figure 3.

©2015. American Geophysical Union. All Rights Reserved.

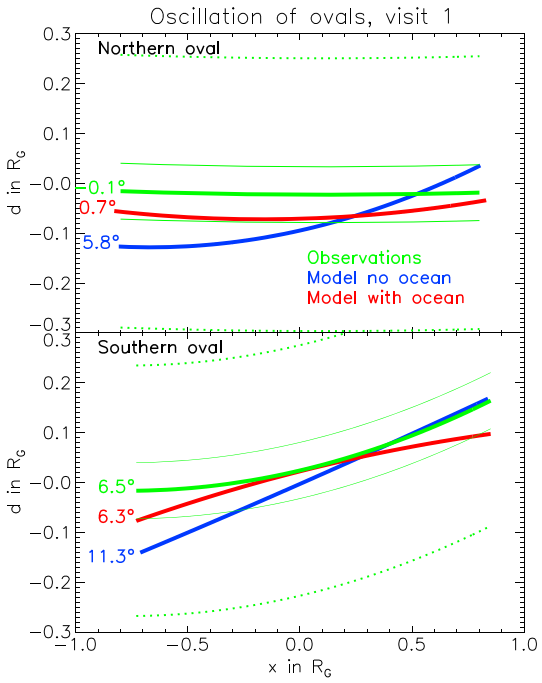

Figure 5. Visit 1: Difference of the ovals $d = y_a - y_b$, when Ganymede is above and below the current sheet for observation and models. Associated rocking angles are indicated. The positions i_{x_E} and i_{x_W} used to calculate the rocking angles are the left and right ends of the polynomial fits, respectively. Formal error ranges (Appendix B) are shown as green dotted lines, and realistic error ranges according to the Monte Carlo model (Appendix C) are shown as thin green lines.

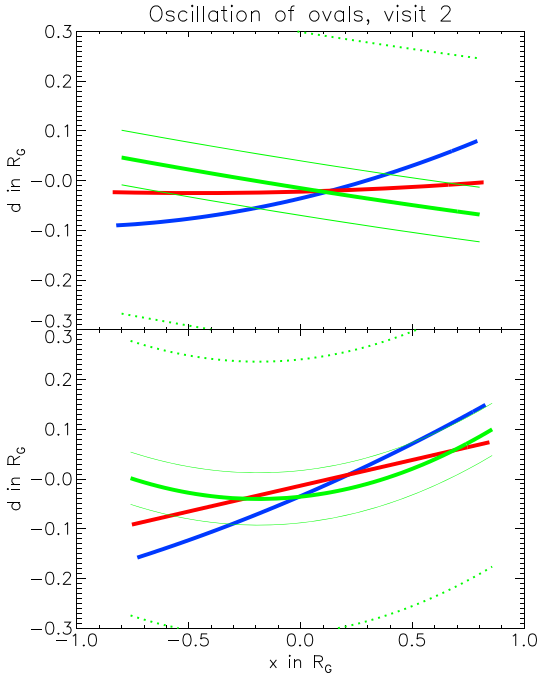

Figure 6. Visit 2: Difference of the ovals $d = y_a - y_b$, when Ganymede is above and below the current sheet for observation and models. Other properties are similar as in Figure 5.

The auroral images in Figures 3 and 4 show, both, systematic and stochastic variability. The stochastic variability is most likely due to a combination of intermittent reconnection occurring at the open-closed field line boundary [*Jia et al.*, 2010; *Eviatar et al.*, 2001] and statistical effects due to the weakness of the auroral signal. Therefore, the locations of the oval $y(i_x)$ are not a smooth line, and we fit the locations with a polynomial of second degree of the form

$$y_{\text{oval}}(i_x) = a_0 + a_1 i_x + a_2 i_x^2 \tag{3}$$

to more easily monitor the systematic temporal evolution of the ovals. Based on the structure of the observed and modeled ovals we find that a polynomial fit of second degree represents the ovals adequately with only a small number of fit parameters. In the polynomial fit the sum of the squared differences between the polynomial and the observation divided by the associated effective width for each i_x is minimized. The effective width is a quantity defined in Appendix B. In Figures 3 and 4, the fitted ovals are shown as dashed and solid green lines when Ganymede was above and below the current sheet, respectively.

To quantitatively determine the change in the locations of the ovals, we introduce the difference

$$d(i_x) = y_a(i_x) - y_b(i_x), \tag{4}$$

where y_a and y_b represent the y coordinates (north-south direction) of the polynomial fit when Ganymede is above and below the current sheet, respectively. The differences $d(i_x)$ for visit 1 and visit 2 are shown in Figures 5 and 6, respectively.

The main objective of the data analysis is to determine how strongly the ovals oscillate up and down when Ganymede is above and below the current sheet. The amplitude of the oscillation can be quantitatively determined with a rocking angle α defined by

$$\tan(\alpha) = \frac{\mathrm{d}(x_W) - \mathrm{d}(x_E)}{x_W - x_E}. \tag{5}$$

The positions x_E and x_W represent the most eastern and western positions on the disk. The northern and southern ovals of visit 1 and visit 2 shown in Figures 3 and 4 represent four independent measurements of the rocking angle α.

©2015. American Geophysical Union. All Rights Reserved.

3. Models of the Magnetic Field Environment

To assess the observed temporal change of the locations, we use a MHD model of the interaction of Ganymede with the plasma of Jupiter's magnetosphere [*Duling et al.*, 2014]. The model includes the time-variable component of Jupiter's magnetospheric field as seen in the rest frame of Ganymede [*Khurana*, 1997; *Connerney et al.*, 1998; *Seufert et al.*, 2011]. Ganymede's internal dynamo field is described with the Gauss coefficients derived in *Kivelson et al.* [2002]. We use either all derived Gauss coefficients from *Kivelson et al.* [2002] in the absence of induced magnetic fields or only dipole moments when induction is included. Induction is calculated with expressions from *Zimmer et al.* [2000] and *Saur et al.* [2010] for an ocean with an assumed electrical conductivity of 0.5 S/m and a thickness of a 100 km. The ocean is assumed to be located at depth between 150 km and 250 km, similar to *Kivelson et al.* [2002]. Earth's oceans in comparison possess a typical electrical conductivity of approximately 5 S/m and a related salinity of 35 grams per kilogram of seawater with the two most abundant cations Na^+ and Mg^{2+} and anions Cl^- and SO_4^{2-} [*Telford*, 1993; *Garrison*, 2006]. The most abundant salt in Ganymede's ocean is expected to be $MgSO_4$ with possible concentrations between 0 gram and 100 grams per kilogram of water [*Vance et al.*, 2014]. Using the conductivity versus concentration curve for $MgSO_4$ for Europa from *Hand and Chyba* [2007], our model conductivity of 0.5 S/m would correspond to 5 grams $MgSO_4$ per kilogram of ocean water. The plasma interaction of Ganymede with Jupiter's magnetosphere includes the following processes: A constant photoionization frequency within Ganymede's oxygen atmosphere, recombination of molecular oxygen ions and electrons, momentum exchanging collisions of the magnetospheric plasma with Ganymede's atmosphere, a prescribed electrical conductivity in Ganymede's ionosphere, an anomalous resistivity near the magnetopause [*Jia et al.*, 2010], and a new consistent description for the magnetic boundary condition at Ganymede's surface. The boundary condition considers the electrically insulating nature of Ganymede's ice crust [*Duling et al.*, 2014]. Note that induction is included in our model within the quasi-stationary assumption similar to the work in *Schilling et al.* [2007, 2008], *Jia et al.* [2009], and *Duling et al.* [2014]. The basis of this assumption is that induction occurs on time scales of 10.5 h and the plasma interaction on scales of approximately 10 min. We first calculate the induced magnetic field signal fully time dependent in response to the external time-variable field including a phase lag caused by an ocean with a finite conductivity. Because the plasma interaction occurs on time scales much shorter compared to the induction time scales, the inductive response is then assumed to be time constant within each individual plasma simulation. A detailed discussion of this approach can be found, e.g., in *Saur et al.* [2010].

We account for four scenarios: Ganymede is above or below the current sheet and possesses a dynamo field with dipole and quadrupole moments or a dynamo dipole field plus induction in an ocean, respectively. From the resultant modeled magnetic fields we calculate the locations of the open-closed field line boundaries mapped onto the disk of Ganymede with the same viewing geometry as in the observations. The four model runs used in this analysis are thus characterized by whether Ganymede possesses an ocean or not and whether Ganymede is above or below the current sheet with magnetospheric background fields B_0 = (0, −86, −79) nT and (0, +86, −79) nT, respectively. Here the x component of the vector field points in the orbital direction of Ganymede, y points toward Jupiter, and z completes a right-handed coordinate system. The upstream plasma velocity with respect to Ganymede is v_0 = 140 km s^{-1} and in the x direction. The upstream plasma density ρ_0 and energy density e_0 contain both systematic (i.e., as a function of magnetic latitude) and stochastic variability (i.e., due to random variability in Jupiter's magnetosphere). Note that no upstream plasma measurements are available for the times when the HST observations were taken. In order to attain a reasonable fit to the observed auroral locations, we chose the following values for visit 1 above the current sheet: ρ_0 = 28 amu cm^{-3} and e_0 = 2.85 nPa; for visit 1 below the current sheet: ρ_0 = 56 amu cm^{-3} and e_0 = 5.7 nPa; and for visit 2 above and below the current sheet: ρ_0 = 56 amu cm^{-3} and e_0 = 11.4 nPa, respectively. Such variability of the upstream conditions during half a rotation period or during the two visits is within observed ranges [*Bagenal and Delamere*, 2011; *Frank and Paterson*, 2000]. All other properties are identical to the properties given in *Duling et al.* [2014].

We use the locations of the open-closed field line boundary (OCFB) on the surface of Ganymede as a model reference for the locations of the ovals [*McGrath et al.*, 2013; *Jia et al.*, 2010]. Therefore, we assume that the auroral emission predominantly stems from an atmospheric molecular oxygen layer directly located near the surface, and we thus neglected the finite vertical extent of the emission. This is a reasonable assumption because the near-surface scale height of an atmosphere in thermal equilibrium with the surface at a temperature of about 100 K is about 20 km. Such a near-surface scale height for Ganymede's oxygen

©2015. American Geophysical Union. All Rights Reserved.

Table 2. Rocking Angles and Associated Properties for the Four Individual Ovals and All Ovals Combined[a]

	North Visit 1	South Visit 1	North Visit 2	South Visit 2	All Combined
α: observation	−0.1	6.5	−4.1	3.5	2.0[b]
σ_α: Appendix B, upper limit	12.7	11.6	14.3	12.6	6.3[c]
α: model ocean	0.7	6.3	0.7	5.9	3.4[d]
α: model no ocean	5.8	11.2	6.0	11.2	8.6[d]
α_{MC}: model with ocean plus patchiness with MC	0.5	3.4	0.3	4.3	2.2[e]
α_{MC}: model no ocean plus patchiness with MC	4.3	6.8	4.3	7.6	5.8[e]
σ_{MC}: model ocean plus patchiness with MC	2.6	2.6	2.5	2.4	1.3[f]
σ_{MC}: model no ocean plus patchiness with MC	2.7	2.6	2.6	2.4	1.3[f]

[a]All values are given in units of degree. MC stands for calculated with the Monte Carlo method.
[b]Calculated with (B6).
[c]Calculated with (B7).
[d]Calculated as arithmetic average.
[e]Calculated with (B6) and expectation values from individual α_{MC} and σ_{MC}.
[f]Calculated with (B7) and expectation values from individual σ_{MC}.

atmosphere has also been modeled by *Marconi* [2007]. With this scale height, 97% of the atmosphere lie within an altitude of ~70 km which corresponds to the size of a pixel on the detector. At altitudes larger than approximately 200–300 km the scale height significantly increases, but atmospheric oxygen densities at these altitudes are already 4 orders of magnitude smaller compared to those at the surface [*Marconi*, 2007]. Because the dilute oxygen atmosphere is "optically thin" for auroral electrons and also optically thin for photons at 1356 Å [*Hall et al.*, 1995, 1998], nearly all the auroral emission indeed stems from very close to the surface, and thus, the vertical extent of the aurora can be neglected in our analysis.

To calculate the location of the OCFB in the MHD models, we follow the magnetic field lines by starting near the surface of Ganymede at a certain planetary longitude for various latitudes. The latitudes of the oval are given by the transitional points between field lines that close on Ganymede and field lines that connect to Jupiter. The numerical resolution of the MHD model is 1.5° in latitudinal and longitudinal directions. The field line tracking is performed with interpolated field values within the grid cells. Due to the strong dipolar component of the field and the resultant smooth fields near the surface, the model OCFB on Ganymede can well be determined down to grid resolution when tracing individual field lines. The average locations of the ovals from the model and the resulting rocking angles, however, can be constrained to much better precision than 1.5° due to statistical reasons, as discussed in section 4.2.

4. Results and Discussion

In this section we first present the results of our analysis of the rocking angles and then discuss the robustness of the rocking angles derived from numerical modeling. We also discuss implications for the subsurface ocean and Ganymede's dynamo.

4.1. Results of the Rocking Analysis

Figures 3 and 4 show the auroral ovals above and below the current sheet for visit 1 and visit 2, respectively. The figures also include the polynomial fit of second degree to the observations shown as green lines. For comparison we show modeled locations of the auroral ovals with the MHD model from *Duling et al.* [2014] when an ocean is included (red lines) and when no ocean is present (blue lines). It should be emphasized that the finite width of the observed ovals is larger than the differences in the locations of the modeled ovals with and without ocean in each individual image. Therefore, it is impossible by simple visual inspection of individual images to separate the ocean from the no-ocean hypothesis. However, we will subsequently show that both hypotheses can still be well separated with the statistical analysis techniques discussed in the remainder of this work. The statistical analyses are based on the collective number of resolution elements within each observed image and the availability of measurements of the northern and southern ovals from two different sets of HST data.

To visualize the displacement of the ovals when Ganymede was above and below the current sheet, we show in Figures 5 and 6 the differences $d(i_x)$ from equation (4). The modeled temporal change of the

©2015. American Geophysical Union. All Rights Reserved.

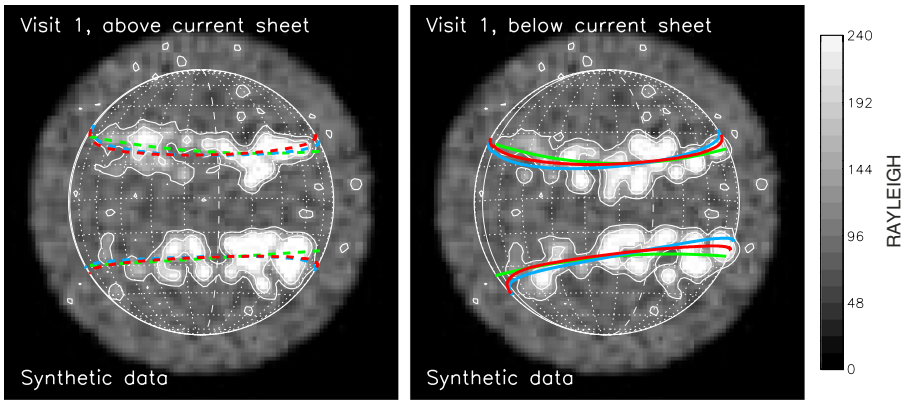

Figure 7. Examples for synthetic auroral emissions in Rayleigh calculated with a Monte Carlo model when an ocean is assumed and Ganymede is (left) above and (right) below current sheet. North is up, and Jupiter is to the right. Green lines display the polynomial fits of second degree to the data, blue lines display modeled locations when no ocean is present, and red lines display model locations when an ocean is present.

locations is stronger in models without an ocean than in models with an ocean (slopes of blues lines are steeper than slopes of red lines in Figures 5 and 6, respectively). The oscillations of the observed locations of the ovals (green lines) are small and comparable to the expected reduced oscillation of the ovals with an ocean present.

The oscillation can quantitatively be assessed with a rocking angle α defined in (5). Four measurements of the rocking angles are obtained from the observations of the northern and southern ovals during the two visits. The values of these measurements are shown in Table 2. The table also includes formal uncertainties of the rocking angles, which are derived in Appendix B. Note that the individual rocking angles from the four independent measurements are expected to be only approximately similar but not identical mostly due to viewing geometry. All four measurements can be considered independent because emission from the northern hemisphere does not influence the emission from the southern hemisphere and vice versa. Equally the emissions from both visits do not influence each other. As an overall measure for the oscillation properties of Ganymede's aurora we introduce an average rocking angle $\bar{\alpha}$ and an average uncertainty $\bar{\sigma}_\alpha$ defined by expressions (B6) and (B7), respectively. From a statistical point of view, each individual rocking angle can be considered a random variable with a certain expectation value and variance. Even though each individual rocking angle does not have exactly the same expectation value, the average rocking angle can be formally introduced as a new random variable with its own statistical properties (such as expectation value and variance). We introduce the average rocking angle for two reasons: (1) It is a single value quantity well suited to test the observations against the ocean and the no-ocean hypotheses and (2) it has an approximately 4 times smaller variance compared to the individual rocking angles. For the average rocking angle we find $\bar{\alpha} = 2.0°$ with a formal uncertainty of $\pm 6.3°$. The expected rocking angles are 3.4° with ocean and 8.6° without ocean derived from the MHD model using the same polynomial fits as in the observations (but prior to the consideration of stochastic effects, which will be discussed next).

The above analysis does not address the effects of the stochastic patchiness of the auroral morphology on the rocking angles. The related formal error analysis also strongly overestimates the uncertainty of the observed rocking angles. One reason is that the formal error analysis includes fluxes on a large area of the disk in the calculation of the effective width $< \tilde{w}_{\text{oval}} >$ of the ovals, i.e., within 5° and 60° latitude (see also Appendix B). The effective width includes, in addition to emission directly from the ovals, a global emission contribution, which is excited by globally abundant 'no-auroral' electrons. Both are difficult to separate unambiguously. Another reason why the formal error analysis in Appendix B strongly overestimates the real error is that it assumes the emissions along the ovals are fully correlated. The formal error calculation assumes an averaged uncertainty $< \tilde{w}_{\text{oval}} >$ of the ovals positions, i.e., that $< \tilde{w}(i_x) >$ are fully correlated for each i_x. If the uncertainties along an oval were uncorrelated for each i_x, the total uncertainty would be reduced by approximately the square root of the number of pixels N along the oval in i_x direction, relative to the uncertainty at an individual pixel i_x. This certainly represents a too extreme assumption. Neighboring

©2015. American Geophysical Union. All Rights Reserved.

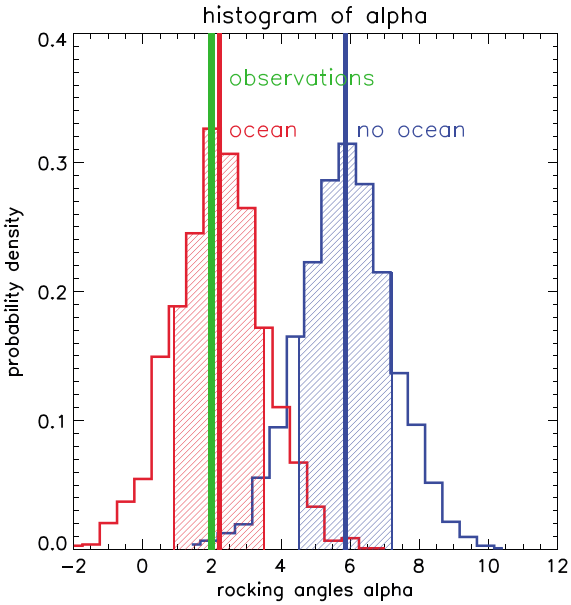

Figure 8. Distribution function of modeled rocking angles $\bar{\alpha}(j_s)$ with and without ocean, respectively, including the effects of stochastic patchiness on the measurements. The vertical green line indicates rocking angle derived from observations. The vertical red and blue lines indicate expectation values $E[\bar{\alpha}]$, and shaded area displays the 1 sigma area around the expectation values.

pixels are correlated to some extent as apparent in the patchy nature of the emissions due to physical correlations and contributions from the data processing such as smoothing and the point spread function. The correlations, however, seem to exist only along a limited fraction of the oval arc. Formally one could calculate the full correlation tensor between each pixel of each exposure and include it in the error analysis. These calculations, however, would get exceedingly complex and will additionally lose transparency.

In cases where the error analysis becomes too complex, a straightforward way to estimate the uncertainty is through a Monte Carlo (MC) method where the errors are estimated from an ensemble of synthetic observations. In the MC test we generate 2048 sets of synthetic HST images based on model runs with and without oceans, respectively, but with randomly generated patchiness and measurement noise comparable to the real observations. Details about how the synthetic images are generated are given in Appendix C. Two examples of synthetic images are shown in Figure 7. These images were created with the MHD model assuming an ocean being present. The underlying model ovals are shown in red. The random patchiness is calculated around these model ovals. For comparison we also show the expected location of the ovals when no ocean was assumed. In Figure 7 we also show the polynomial fits to the patchy synthetic images as green lines. They are calculated in exactly the same way as for the real data.

Subsequently we also apply the same procedure that we apply to the real data to the synthetic images in order to determine the rocking angle $\bar{\alpha}$ and uncertainty $\bar{\sigma}$. The resultant distribution function for $\bar{\alpha}$ is shown in Figure 8. The expectation values $E[\bar{\alpha}]$ are reduced to 2.2° with ocean and 5.8° without ocean compared to the model results without patchiness given above (see also Table 2). The probability distribution functions of the averaged rocking angles $\bar{\alpha}$ with and without ocean only weakly overlap, which implies that both hypotheses can generally be separated. The associated variances for both the ocean and no ocean models are $V[\bar{\alpha}] = \bar{\sigma}^2_{\mathrm{MC}} = (1.3°)^2$. The resultant $\bar{\sigma}^2_{\mathrm{MC}}$ can be considered a measure for the uncertainty of the observed rocking angle. They are smaller than the formal errors calculated with the error propagation method described in Appendix B. The observed $\alpha = 2.0° \pm 1.3°$ is consistent with the presence of an ocean, whereas its absence is highly unlikely with a probability smaller than 1%.

As a result of randomly distributed spots along the ovals, the derived rocking angles from the MC test varies for each numerical realization. In some cases the rocking angle can even turn negative depending on how the random patches are distributed (see Table 2). Note that the probability distribution functions of the rocking angles for the individual ovals are roughly twice as wide as the distribution function for the averaged rocking angle from all four ovals shown in Figure 8. This increases the likelihood of an individual α to turn negative.

As stated before, the finite width of the observed ovals is larger than the differences in the locations of the modeled ovals with and without ocean in each individual image. This precludes a simple visual inspection of individual images to separate the ocean from the no-ocean hypothesis. Both hypotheses, however, still can be separated for two reasons. (1) Four independent measurements of northern and southern ovals from two visits are available. This reduces the error approximately by a factor of $1/\sqrt{4}$. (2) Additionally, the pixels along the ovals are not fully correlated, and thus, each vertical column of pixels along the ovals represents

©2015. American Geophysical Union. All Rights Reserved.

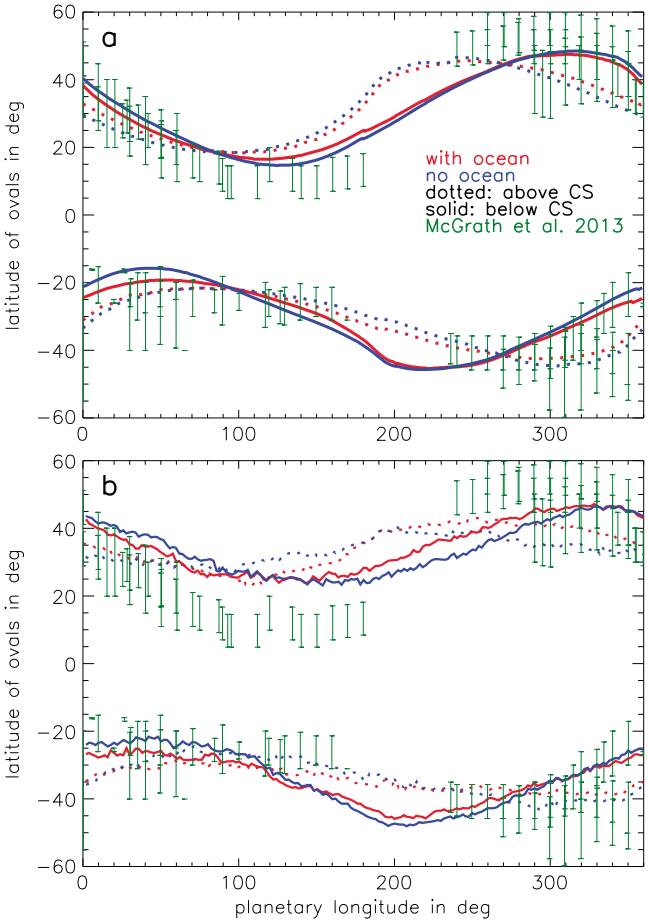

Figure 9. Modeled locations of the ovals with and without ocean (red and blue curves, respectively) from two different models when Ganymede was above and below the current sheet (dashed and solid, respectively): (a) Calculated ovals with the model by *Duling et al.* [2014]. Model calculations are from runs with upstream thermal and kinetic plasma pressures 5.7 nPa and 1.8 nPa, respectively. (b) Locations calculated with a model from *Jia et al.* [2009] for an upstream thermal pressure of 1.9 nPa and ram pressure of 0.9 nPa. Both panels show that the presence of an ocean reduces the oscillations of the ovals compared to the case when no ocean is present. Panels include observations from *McGrath et al.* [2013] (green) for comparison of the general structure only. They were taken at times when Ganymede was at different orbital positions and at different positions with respect to the current sheet compared to the observations and models analyzed in this paper.

partially independent measurements as well. This effect additionally reduces the uncertainty by a factor of 1.3°/6.3° = 1/4.8, based on the ratio of uncertainties from the formal error calculation and the MC test (values of both uncertainties are given in Table 2).

4.2. Model Robustness

An important question of our analysis is whether the amplitude differences of the auroral oscillation with and without ocean are model dependent. Therefore, we investigate both the impact of different upstream conditions of Jupiter's magnetosphere and the impact of different MHD models. For the latter we compare the locations of the open-closed field line boundary (OCFB) calculated with the models by *Duling et al.* [2014] and with those calculated from the independent model by *Jia et al.* [2009], introduced in detail further below.

Two examples of the locations of the OCFB are shown in Figure 9 in normal cylindrical projections. Figure 9a shows the OCFB calculated with the model by *Duling et al.* [2014] with upstream thermal and kinetic plasma pressures 5.7 nPa and 1.8 nPa, respectively. The latitudinal and longitudinal numerical resolution is 1.5°. The jitter/variability of the locations of the ovals is on average even smaller. The uncertainty in tracking the OCFB can be approximated by the numerical resolution of the models used. Figure 9b shows the OCFB from an entirely independent MHD model of Ganymede's magnetic field environment by *Jia et al.* [2009]. Many physical properties of this model are similar to the ones developed in *Duling et al.* [2014]. Both models include the internal dynamo field [*Kivelson et al.*, 2002] and can take into account induction in a subsurface ocean. They both reproduce the in situ magnetic field measurements by the Galileo spacecraft remarkably well. The Jia model does not explicitly include an atmosphere and ionosphere. In order to account for the electrically nonconductive nature of Ganymede's surface, the induction equation is solved within Ganymede in the Jia model. For numerical reasons the conductivity jump across the surface of Ganymede needs to be smoothed in the Jia model. The resultant current close to the surface of Ganymede is argued to represent ionospheric currents in the Jia model. In contrast, the ionospheric currents are explicitly included in the Duling model. The upstream magnetic field and velocity values are similar in all model runs used here. The plasma conditions in the Jia model runs used in this work are from *Jia et al.* [2009] with values of $\rho_0 = 28$ amu cm^{-3} and p = 1.9 nPa, i.e., smaller values compared to the other runs shown in this paper (see also Figure 10).

©2015. American Geophysical Union. All Rights Reserved.

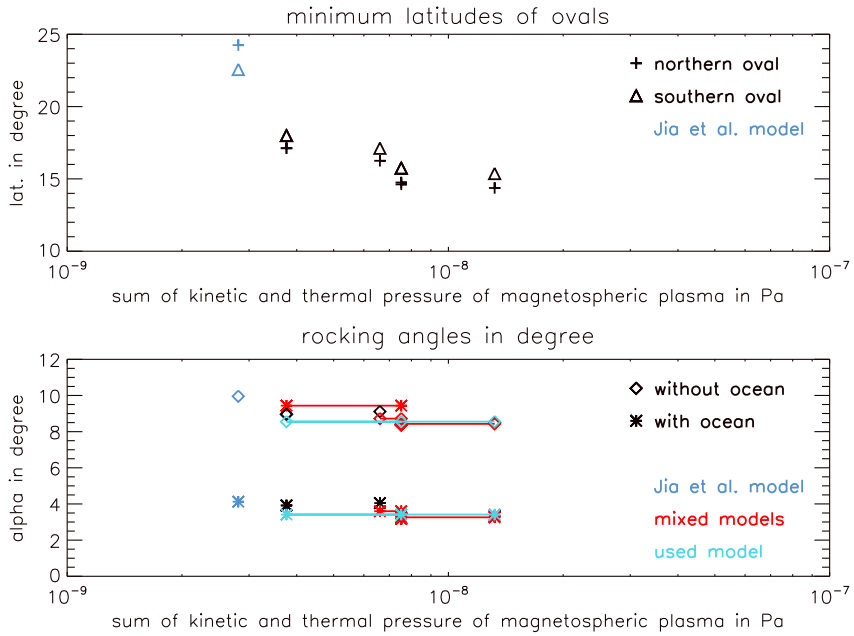

Figure 10. (top) Minimum latitude of ovals and (bottom) average amplitudes of oscillation with and without ocean for different values of upstream pressure and two different MHD models. The blue symbols for the smallest upstream pressure are from runs with the model by *Jia et al.* [2009]. The black symbols are from runs with the model by *Duling et al.* [2014]. Turquoise symbols are from the runs used for direct comparison with the HST data where the upstream conditions have been allowed to be different. Red symbols represent examples of other selected mixed models, i.e., when different upstream conditions have been chosen for cases when Ganymede was above and below the current sheet.

The location of the ovals obtained from the Jia model shows scatter on the order of 2°, similar to the resolution applied to calculate the OCFB with this model. In addition, there is variability due to the nonsmooth magnetic field structure near the reconnection point. However, the amplitude differences in the locations of the ovals with and without ocean is up to 3°–5° in both models and larger than the scatter in the modeled ovals (see Figure 9: runs with ocean as red curves, runs without ocean as blue curves, and Ganymede above and below the current sheet as solid and dashed lines, respectively). An important conclusion from the results shown in Figure 9 is that both models predict measurably less oscillation when an ocean is present compared to when no ocean is present. It thus demonstrates that the predicted differences do not depend on the underlying MHD model.

It needs to be stressed that the differentiation of the models with and without ocean is based on the entire length of the oval's imprint on each hemisphere through a polynomial fit and not single oval data points. Therefore, the ovals only need to be separated on average. To investigate the separability of both hypotheses, we apply the MC test, where we add significantly more patchiness to the data than the jitter in modeled ovals, adjusting the patchiness of model images to the observed level.

In Figure 9 we also compare our modeled locations with the observed average locations of Ganymede's oval from an analysis by *McGrath et al.* [2013] when Ganymede was at different orbital positions and at different positions with respect to Jupiter's plasma sheet compared to the model runs of this analysis. We nevertheless include the data comparison to demonstrate that our model reproduces key features of the aurora; i.e., the ovals are significantly closer to Ganymede's magnetic equator on the downstream side (around 90° west longitude) compared to the upstream side (around 270°). A detailed comparison of the locations from the Jia model and the previous HST observations is presented in *McGrath et al.* [2013]. Note that because of the selected position of Ganymede with respect to the plasma sheet, the observations presented in *McGrath et al.* [2013] are not suited to address the ocean question. The error bars in the extracted locations of the ovals in *McGrath et al.* [2013] are significant, similar to the finite width of the ovals of the current observations. In this context, it is important to stress again that based on one single set of ovals where the errors bars along the ovals are assumed to be fully correlated, the ocean models cannot be

©2015. American Geophysical Union. All Rights Reserved.

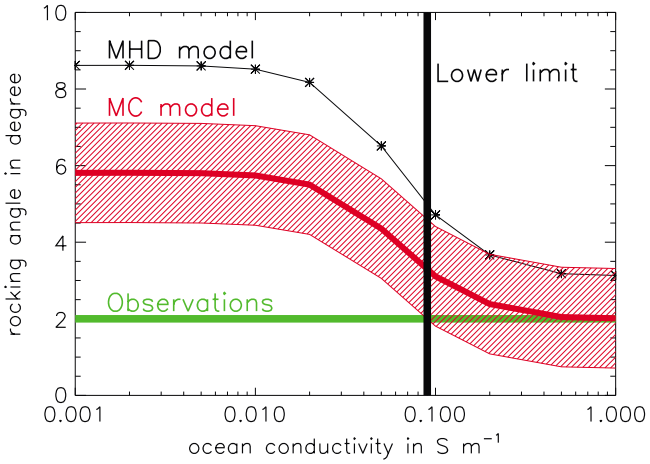

Figure 11. Rocking angle $\bar{\alpha}$ as a function of ocean conductivity for an ocean located between 150 km and 250 km depth. The green curve displays the rocking angle extracted from the observations. The black curve shows the rocking angle calculated with the MHD model of *Duling et al.* [2014]. The red curve and shaded area represent the rocking angle and the related uncertainties from the Monte Carlo modeling, respectively. Most of the latter values are derived from the MHD modeling by a scaling law (see main text). Black vertical line shows the lower limit for ocean conductivity such that the modeled rocking angles are still in agreement with the observations.

separated from the no-ocean models. It is the combination of having four independent measurements of the movements of the ovals and the partial decorrelation of the uncertainties along the ovals which enables the separations presented here (see also detailed discussion in Appendix C).

In order to investigate the sensitivity of the amplitude differences of the oscillations with and without ocean for different models and model parameters, we performed a series of model runs, where we varied the upstream plasma pressure. During the times of the HST observations no independent measurements of the plasma pressure were available. In our study we investigate the effects of the total upstream pressure defined as sum of ram and thermal pressure. In Figure 10 (top) we show the minimum latitudes of the ovals when no ocean is assumed. The minimum latitudes of the ovals decrease from nearly 25° to approximately 15°, as expected, as a function of increasing upstream plasma pressure. This effect is similar to the variability of Earth's auroral ovals under increasing solar wind pressure. The blue symbols are from the independent model by *Jia et al.* [2009]. In Figure 10 (bottom) we show the extracted oscillations of the ovals when Ganymede is above and below the current sheet. For all upstream plasma pressures, the expected amplitudes of the oscillation are between 8° and 10° when no ocean is present. With an ocean present the amplitudes of the oscillations are reduced to approximately 4° for all upstream plasma conditions. This holds also for the independent model of *Jia et al.* [2009]. The plasma pressure controls the absolute latitudinal positions of the ovals, but it has very little effect on the oscillations of the ovals with and without ocean. Thus, both properties of the ovals are independent, and the amplitudes of the oscillations of the ovals in response to externally changing fields are indeed diagnostic of the internal conductivity structure of Ganymede.

As argued by several authors [*McGrath et al.*, 2013; *Jia et al.*, 2009, 2010; *Eviatar et al.*, 2001], the locations where the OCFB intersect with the surface/atmosphere of Ganymede correspond to the location of the auroral ovals. For example, MHD modeling by *Jia et al.* [2010] shows that shear flow near the OCFB drives strong and localized electric currents along the OCFB, which are likely the root cause for the auroral emission similar to the discrete aurora at Earth. However, if the OCFB only approximately represents the locations of the ovals, then a resultant distance Δy between the latter and the oval exists. If we reasonably assume that Δy is similar when Ganymede is above the current sheet and below the current sheet, the difference $d(x)$ introduced to measure the oscillation of the ovals can still be obtained from the OCFB with good approximation.

We also applied simpler semianalytical models, where the magnetic field contributions from the plasma interaction have been calculated using a wire model. In the wire model, line currents along the magnetopause (similar to Chapman-Ferraro currents) and line currents continued along the Alfvén wings have been assumed, where the total currents in the wire loops have been calculated with expressions from *Neubauer* [1998] and *Saur* [2004]. All other contributors to Ganymede's magnetic field environment have been described similar to the full MHD model of *Duling et al.* [2014] applied here. These simpler semianalytic models lead to very similar dependences as derived with the fully consistent MHD models: With increasing strength of the plasma interaction, i.e., increasing total electric current, the locations of the ovals move toward the equator on the downstream side and away from the equator on the upstream side. The

©2015. American Geophysical Union. All Rights Reserved.

amplitudes of the oscillations with and without ocean are, however, barely affected by the interaction strength.

We note that Ganymede's atmosphere likely contains deviations from radial symmetry as modeled, for example, by *Marconi* [2007] and *Plainaki et al.* [2015]. The atmosphere and its structure influences the plasma interaction. However, even though we did not perform runs with nonsymmetric atmospheres, we generally expect its effects on the properties of the oscillation amplitudes to be small because we generally only see a weak influence of the plasma interaction on the oscillation differences with and without ocean (as discussed earlier in this subsection).

4.3. Properties of the Ocean

The model rocking angle increases when the ocean conductivity is reduced. In our modeling we find that a conductivity σ of 0.09 S/m for an ocean assumed to be located between 150 km and 250 km depth provides a lower limit for the model ovals still being consistent with the observations within the uncertainties from the MC test (see Figure 11). This lower limit has been derived from a series of MHD model runs also shown in Figure 11 with variable ocean conductivities σ within 1×10^{-3} S/m to 1 S/m. The resultant rocking angle $\bar{\alpha}$ is shown as thin black line marked with crosses. Because the evaluations of the rocking angles from the MC test is numerically expensive, we scaled the rocking angles from the MHD model α_{MHD} to obtain the rocking angles α_{MC} according to the MC test based on the rocking angles at zero conductivity (i.e, no ocean) and 0.5 S/m. Values for the rocking angles for these two conductivities are given in Table 2. We applied the linear scaling

$$\alpha_{\mathrm{MC}}(\sigma) = \alpha_{\mathrm{MC}}(0\ \mathrm{S}) + \frac{\alpha_{\mathrm{MC}}(0\ \mathrm{S}) - \alpha_{\mathrm{MC}}(0.5\ \mathrm{S})}{\alpha_{\mathrm{MHD}}(0\ \mathrm{S}) - \alpha_{\mathrm{MHD}}(0.5\ \mathrm{S})}(\alpha_{\mathrm{MHD}}(\sigma) - \alpha_{\mathrm{MHD}}(0\ \mathrm{S}))\ , \tag{6}$$

leading to the rocking angle for the MC test for varying conductivities σ (shown as the red curve in Figure 11). The resultant uncertainty is assumed to be 1.3° for every σ similar to the uncertainties of 1.3° derived for 0 S/m and 0.5 S/m (see Table 2). The uncertainty is displayed as red-shaded region in Figure 11. The modeled rocking angles from the MC test within the 1 sigma uncertainty are in agreement with the rocking angle derived from the observations shown as green horizontal line for conductivities larger than 0.09 S/m. These values represent thus a lower limit for the ocean conductivity. For lower conductivities the green curve (observations) no longer overlaps with model expectations (red area). Using the conductivity versus concentration curve for $MgSO_4$ for Europa from *Hand and Chyba* [2007], a minimum conductivity of 0.09 S/m would correspond to a minimum salt concentration of 0.9 gram $MgSO_4$ per kilogram of ocean water.

Note that to a good approximation for small ocean thicknesses H compared to Ganymede's radius R_G and the same average ocean location within Ganymede all modeling runs with the same depth-integrated conductivity $\Sigma = \sigma H$ are equivalent. Thus, any combination of σ and H (under the $H/R \ll 1$ assumption and realistic σ) with values larger than 100 km × 0.09 S/m is consistent with the HST observations (assuming that the average location of the ocean is at a depth of 200 km). Deviations from this law occur when the thickness and the conductivity of the ocean are large. Such deviations are, for example, visible in Figures 11 and 12 of *Seufert et al.* [2011] near regions where the isolines of Ganymede's induction amplitude are not linear anymore.

The lower limit for the conductivity can be alternatively used to calculate a maximum depth of the ocean. An ocean at depth between 150 km and 250 km with conductivity 0.09 S/m generates an induction amplitude of $A = 0.8$ (calculated with expressions in *Saur et al.* [2010]). A similar amplitude would be generated by a perfectly conductive ocean at a depth of 330 km. Any less conductive ocean needs to be located closer to the surface of Ganymede. Note that in this simple equivalence estimate, the effect of the phase shift has been neglected. We also note that our estimation of the maximum depth to the ocean is consistent with theoretical expectations. At depths greater than approximately 150 km in Ganymede, the low-pressure form of ice (ice I_h) is expected to be replaced by high-pressure polymorphs, whose melting temperature increases with pressure, whereas for ice I_h it decreases with pressure. Therefore, the top of an ocean, if it exists, is expected to be most likely at a depth of 150 km or less [e.g., *Vance et al.*, 2014].

4.4. Implication for the Dynamo Field

In the absence of an induced magnetic field a small intrinsic quadrupole component is needed to explain the Galileo magnetic field measurements, yet this component is not required if a conducting ocean is present [*Kivelson et al.*, 2002]. We may therefore consider the ratio of power [*Langel and Estes*, 1982] of the

©2015. American Geophysical Union. All Rights Reserved.

quadrupole to that of the dipole $R_2/R_1 = 0.0025$ of the oceanless field model as the upper limit for the actual intrinsic field of Ganymede, given that our results demonstrate that an induced component is present. At the top of Ganymede's iron core, whose radius is probably at least 650 km [*Sohl et al.*, 2002], the ratio of quadrupole to dipole power turns out to be < 0.04. This is the lowest ratio of all known dynamo fields at the surface of the dynamo region, with the possible exception of Saturn's magnetic field.

This suggests that a unique dynamo is at work. Possible reasons could be that Ganymede's dynamo might operate close to the critical Rayleigh number for dynamo onset due to its small size, that it operates in Jupiter's field [*Levy*, 1979; *Gómez-Pérez and Wicht*, 2010] or that it is driven by "iron snow" forming below the core-mantle boundary *Hauck et al.* [2006]. In particular, the iron snow scenario appears promising. If Ganymede's core contains more than a few percent of sulfur, crystallization of iron would start at the top of the core [*Williams*, 2009], with iron snow sinking and dissolving at greater depth where the associated iron enrichment of the core alloy drives composition convection. The snow-forming top layer develops a gradient in sulfur concentration and becomes stably stratified. Numerical dynamo simulations show that the presence of the stable layer above the dynamo can strongly reduce the quadrupole-to-dipole ratio [*Christensen*, 2015].

5. Summary and Discussion

In this work we present a new means to search for a saline electrically conductive ocean within Ganymede based on observations and modeling of the locations of Ganymede's auroral ovals. We analyze HST observations of Ganymede's auroral ovals to measure how the locations of its ovals respond to Jupiter's time-periodic magnetic field. For this investigation, two dedicated HST visits of approximately 7 h each were executed to observe Ganymede experiencing the maximum time variability of Jupiter's magnetospheric field. We find that the ovals only weakly oscillate in response to the external time-periodic field with an average amplitude of 2.0°. We also performed three-dimensional simulations of Ganymede's magnetic field environment for various upstream plasma conditions and with two entirely independent MHD models from *Duling et al.* [2014] and *Jia et al.* [2009] to investigate the effects of a saline, electrically conductive subsurface ocean on the time variability of the oval's locations. With these models, we consistently find that the time-variable external magnetic fields generate secondary magnetic fields in a conductive ocean that reduce the oscillation of the ovals to approximately 4°. If no ocean is present, the models predict an oscillation of approximately 8° to 10°.

In addition to the systematic variability, the observed ovals contain also a stochastic variability most likely caused by intermittent reconnection [*Jia et al.*, 2010]. We model the stochastic variability as a random process and generate synthetic images with patchiness comparable to those of the real observations. With a large set of randomly generated synthetic images we perform a Monte Carlo test to investigate if the ocean and the no-ocean hypotheses can statistically be separated based on the current set of observations. The MC test shows that the distribution function of the rocking angles from both hypotheses barely overlap and that the two hypotheses can thus in the great majority of cases be well separated. The patchiness smears out the slope of the ovals and thus leads to a reduction of the rocking angles compared to the MHD simulations. The expectation value from the MC test for the rocking angle with ocean is 2.2° while the rocking angle without ocean is 5.8° with an uncertainty derived from the MC test of 1.3°. The observed rocking angle of 2.0° thus is well consistent with the ocean model and is inconsistent with the absence of an ocean keeping in mind the assumptions and uncertainties that went into the analysis. In addition to the in situ measurements from the Galileo spacecraft [*Kivelson et al.*, 2002], our observations provide further evidence for the existence of a subsurface ocean. The current method uses two-dimensional explicit time-dependent telescope observations, which are not subject to the nonuniqueness issue of spacecraft measurements along single trajectories taken at separate times.

The modeled ovals are most consistent with a conductivity equal to or greater than 0.5 S/m but require at least a minimum conductivity of 0.09 S/m for an ocean between 150 km and 250 km depth (cf. Figure 11). Alternatively, if the ocean is assumed to be perfectly conductive, the observations require a maximum depth of the top of a perfectly conducting ocean of 330 km. According to *Hand and Chyba* [2007], the conductivities 0.5 S/m and 0.09 S/m correspond to a salt concentration of 5 grams and 0.9 gram $MgSO_4$ per kilogram of ocean water, respectively. The existence of an induced magnetic field signal within Ganymede also suggests that the uniquely low quadrupole to dipole moment ratio derived by *Kivelson et al.* [2002] must be

©2015. American Geophysical Union. All Rights Reserved.

considered an upper limit. Ganymede therefore possesses a unique dynamo, possibly driven by iron snow near the core-mantle boundary as suggested by *Christensen* [2015].

The observations contain stochastic variability which deserves to be investigated in further studies. This should lead to a better understanding of the processes near the open-closed field line boundary and the kinetic processes which cause the acceleration of the electrons exciting the auroral emissions. Such studies are, however, beyond the scope of this work. The uncertainties of the results presented in this study can be improved with future HST observations or observations by the ultraviolet spectrograph instrument onboard of the Jupiter Icy Moons Explorer (JUICE) mission designed to orbit Ganymede. Magnetometer measurements during the Ganymede orbiting phase of JUICE will also establish the precise amplitude of the induced field component and its phase shift, as well as the intrinsic quadrupole moment of Ganymede.

The method introduced here can also be applied to other planetary moons and planets to study their electrical conductivity structure. If these bodies are exposed to time-variable magnetic fields and exhibit auroral emissions, then their auroral patterns will be modified by any electrically conductive layers. Observations of the auroral emission responses combined with appropriate models for the responses will provide valuable information about these conductive layers, such as subsurface oceans. The method might one day even be applicable to exoplanets (and exomoons); once appropriate objects and associated magnetic fields are observationally confirmed.

Appendix A: Aspects of the Data Analysis

In this appendix we discuss an alternative version to smooth the data and two alternative versions to determine the locations of the ovals. Based on a comparison of their performance, we then justify the usage of the finally applied versions. We also discuss various ways to compare the observed ovals to the modeled ovals.

A1. Data Smoothing

Alternatively to the star filter introduced in section 2.1, we applied a boxcar filter of the form

$$f_B(i_x,i_y)=\frac{1}{9}\left(f(i_x+1,i_y+1)+f(i_x,i_y+1)+f(i_x-1,i_y+1)+f(i_x+1,i_y)+f(i_x,i_y)+f(i_x-1,i_y)\right.$$
$$\left.+f(i_x+1,i_y-1)+f(i_x,i_y-1)+f(i_x-1,i_y-1)\right) \quad \text{(A1)}$$

to smooth the data.

A2. Location of the Ovals

Three methods to determine the locations of the auroral ovals have been tested: (a) Usage of the weighted flux method within 80% of the maximum emission as described in section 2, (b) usage of the brightest pixel in y direction for each i_x, and (c) usage of the average flux-weighted position given by $y(i_x)=\sum_{i_y}(i_y f(i_x,i_y))/\sum_{i_y} f(i_x,i_y)$ within 5°–60° northern and southern latitude.

The advantage of method (b) is that it is simple and straightforward; however, it discards all other information of the fluxes related to the ovals. Method (c) considers all fluxes of a large area of the disk, but it is not suited in our case. The reason is that the auroral emission from Ganymede not only includes emission from the auroral ovals but also emission from everywhere in Ganymede's atmosphere. This emission is due to electron impact excited emission not directly related to the auroral acceleration processes, e.g., due to electrons from Jupiter's magnetosphere. Note that resonance scattering of solar OI 1356 Å photons is negligible [e.g., *Hall et al.*, 1998]. The nonoval-related emission will artificially reduce the rocking of the ovals. A simple example, which illustrates this effect, is the following: Assume an oval with brightness γ lies on a diagonal of a square with length one and the square is filled with homogeneous atmospheric emission with brightness β; i.e., the flux is given by $f(x,y)=\gamma\delta(x-y)+\beta$, where δ is the delta function. Applying method (c) and replacing the sum by an integral leads to the position of the oval given by $y(x)=(\gamma\, x+\beta/2)/(\gamma+\beta)$. The extracted slope of the ovals is therefore $m=\gamma/(\gamma+\beta)$. If the background β is very small, a slope with value $m=1$ would be recovered, but if the background β gets large, the slope turns flat ($m<1$); i.e., the rocking amplitude is artificially reduced due to inclusion of the background. Therefore, we discard this method.

Method (a) combines the advantages of methods (b) and (c). It considers the fluxes in the y direction exceeding a cutoff level of 80% of the brightest pixel for each i_y and thus considers the emission in the

©2015. American Geophysical Union. All Rights Reserved.

Table A1. Rocking Angle in Degree for Different Methods to Determine the Location of the Ovals and Smoothing Procedures[a]

Smoothing Cycle	Brightest Pixel Method (a) Star Smooth	Brightest Pixel Method (a) Box Smooth	Weighted Flux Method Method (b) Star Smooth	Weighted Flux Method Method (b) Box Smooth
0	1.4	1.4	1.5	1.5
1	2.1	1.2	1.6	1.8
2	2.3	1.9	1.6	1.8
3	2.4	2.5	2.0	2.1
4	2.3		2.0*	
5	2.4		2.0	
6	2.1		2.0	

[a]The combination indicated by an asterisk is chosen in this paper.

vicinity of the peak emissions of the ovals, but it discards the effects of the background. The 80% value for the cutoff was deliberately chosen high to clearly separate the emission from the oval compared to other emissions.

The choice of the different smoothing filters and the different methods to determine the locations of the ovals have been investigated on the observations, and their results on the rocking angle have been measured. The resultant values for the average rocking angle are displayed in Table A1.

The brightest pixel method (b) converges less strongly to a stable value for the rocking angle as a function of the smoothing iterations. The smoothing with the star filter leads to slightly better converging properties compared to the boxcar filter, which combines fluxes within 3×3 bins. Note that the relative weight of the coefficients in the boxcar filter has much stronger smoothing power compared to the star filter. Therefore, less smoothing cycles are required for the boxcar filter compared to the star filter to achieve similar levels of smoothing. Based on the results of our test we applied method (a) to images which have been smoothed 4 times by the star filter. This leads to an average rocking angle of 2.0°.

A3. Strategy for Comparison of Observed Ovals to Model Ovals

We fit the observed auroral structure to a polynomial of second degree (see equation (3)). We use the polynomial for its simplicity to compare the positions of the observed ovals to the position of the model ovals. This comparison could in principle be done in various ways. The observations are available on a disk, and the model predictions are provided on the surface of Ganymede, i.e., on a sphere. Thus, the comparison can be done either on the disk by mapping the modeled locations onto the disk or on the sphere by mapping the observation onto this sphere. Projection of the observations onto a sphere suffers from large uncertainties near the edge of the disk, while the projection from the sphere onto the disk does not generate large mapping uncertainties. Therefore, we compare observations and model on the disk.

Another question is what is a reasonable fit function to characterize an oval and its associated oscillation. A useful fit function on the sphere might be a small circle with three fit parameters (radius and center coordinates of small circle). To characterize the observations with the fit function, the fit function needs to be projected onto the disk where it can be constrained with a least mean squares fit to the observations. The projection of the fit function from the sphere onto the disk can generate curves which fit the data nearly equally; e.g., in case of a small circle, a larger radius can be partly compensated by a shifted position of its center. To avoid this possible nonuniqueness effect, we fit the data to one of the most simple and robust fitting functions, a polynomial of second degree on the disk. This function does not describe possible bends near the edge of the disk as well as other fit functions might do. This effect is not necessarily a disadvantage because near the edge of the disk projection effects generally increase the uncertainty of the fitting significantly. At the edge of the disk the polynomial fit is not very sensitive and thus rather robust against projection uncertainties.

An alternative way to compare observations to model data would be to entirely avoid a fit function. Instead, the MHD simulations could be directly projected onto the disk and compared to the observations with a least mean squares fit. This would minimize projection effects as well. However, it has the disadvantage that the comparison is additionally sensitive to the absolute latitudinal positions of the ovals. This method would

©2015. American Geophysical Union. All Rights Reserved.

thus mix effects due to oscillation with effects due to latitudinal position. As we have shown in section 4.2, the absolute position of the ovals and the oscillation of the ovals are largely independent. Finally, the introduction of a fit function has another advantage. It allows to define a rocking angle in a straight forward fashion, which is the quantity used in this analysis to discriminate the ocean and the no-ocean hypotheses and which is further used to constrain properties of the ocean.

Appendix B: Formal Error Analysis

Formal estimates of the uncertainties of the rocking angles are calculated with the following procedure: We denote the processed photon flux per pixel by $f(i_x, i_y)$, after removal of the background and surface-reflected solar light. Each pixel is characterized by integral numbers denoting the positions i_x and i_y. The y location for an individual oval is chosen using the weighted flux method described in section 2.2. The width of an oval in y direction as a function of i_x is calculated by

$$w(i_x) = \left(\frac{\sum_{i_y} (y(i_x) - i_y)^2 \, f(i_x, i_y)}{\sum_{i_y} f(i_x, i_y)} \right)^{1/2} . \tag{B1}$$

The width of the oval $w(i_x)$ at a certain longitudinal position i_x has an additional uncertainty due to the finite count rate in each pixel. The signal-to-noise ratio for a pixel is given by $s/n = (S - B)/(S + B)^{1/2}$ with the total counts S, the counts B of the background flux including the counts of the reflected light and those due to the dark count rate. The statistical uncertainty for the flux in each pixel therefore reads $\sigma_f(i_x, i_y) = f(i_x, i_y)/(s/n)$. The resultant uncertainty of the width $w(i_x)$ of the oval defined in equation (B1) can be calculated by standard error propagations [e.g., *Bevington and Robinson*, 2003]

$$\sigma_w^2(i_x) = \sum_{i_y} \sigma_f^2(i_x, i_y) \left(\frac{\partial w}{\partial f(i_x, i_y)} \right)^2 . \tag{B2}$$

Inserting the derivatives of equation (B1) into (B2) leads to

$$\sigma_w(i_x) = \left[\sum_{i_y} \sigma_f^2(i_x, i_y) \left(\frac{1}{2w} \frac{1}{\sum_{i'_y} f(i_x, i'_y)} \left\{ (y - i_y)^2 - w^2 \right\} \right)^2 \right]^{1/2} . \tag{B3}$$

The total uncertainty in the location of the ovals, i.e., the effective width $\tilde{w}$ of the ovals can be calculated from the measured width w and the uncertainty due to the finite signal-to-noise ratio in each pixel σ_w assuming that both are independent by

$$\tilde{w}(i_x) = \left(w^2(i_x) + \sigma_w^2(i_x) \right)^{1/2} . \tag{B4}$$

The effective width represents the uncertainty of the location of the ovals, which introduces an uncertainty of the rocking angle α. The rocking angle α is determined from the polynomial fit, in which the observed fluxes at all i_x in the auroral band are used instead of using the individual locations $y(i_x)$ at the most eastern and western locations i_{x_E} and i_{x_W}, respectively. Thus, all values, i.e., approximately 60–70, along the oval contribute to the angle α. Similarly, we also use the averaged uncertainty $< \tilde{w}_{\text{oval}} >= \sum_{i_x=i_{x_E}}^{i_x=i_{x_W}} \tilde{w}(i_x)/(i_{x_W} - i_{x_E})$ averaged all along an oval instead of the uncertainty at the most eastern and western positions i_{x_E} and i_{x_W} only. Using error propagation in (5), we can calculate the uncertainty of the angle α defined by

$$\sigma_\alpha^2 = 2 \left(\frac{1}{1 + \tan^2 \alpha} \right)^2 \left(\frac{1}{i_{x_W} - i_{x_E}} \right)^2 \left[\left\langle \tilde{w}^a_{\text{oval}} \right\rangle^2 + \left\langle \tilde{w}^b_{\text{oval}} \right\rangle^2 \right] , \tag{B5}$$

where $< \tilde{w}^a_{\text{oval}} >$ and $< \tilde{w}^b_{\text{oval}} >$ are the average uncertainty of the location of the ovals y^a_{oval} and y^b_{oval}, respectively.

We have four measurements $j = 1, \ldots, 4$ of the rocking angle α_j with their associated uncertainties $\sigma_{\alpha,j}$ originating from the independent measurements of the northern and southern ovals during visit 1 and visit

©2015. American Geophysical Union. All Rights Reserved.

2, respectively. The average rocking angle derived from all four measurements is

$$\bar{\alpha} = \frac{\sum_j \alpha_j/(\sigma_{\alpha,j})^2}{\sum_j 1/(\sigma_{\alpha,j})^2} \tag{B6}$$

with an associated average uncertainty

$$\bar{\sigma}_\alpha = \frac{1}{\sqrt{\sum_j 1/(\sigma_{\alpha,j})^2}} . \tag{B7}$$

Appendix C: Monte Carlo Test and Generation of Synthetic Data

For the MC test we generate 2048 sets of synthetic HST images j_s. We add randomly generated patchiness and measurement noise comparable to that in the real observations to the locations of the ovals obtained from the MHD model with and without ocean. Each set j_s is generated for the same conditions, i.e., apparent size of Ganymede and phase angle as the real observations, and represents a particular realization of possible auroral emission measurement. The patchy structure of the auroral morphology as well as the observed disturbed magnetic field signatures in the vicinity of Ganymede's open-closed field region as discussed in *Jia et al.* [2010] suggests that the substructure of the aurora can be approximated as a random process. We include the patchiness of the ovals in synthetic images with the following procedure: A random generator picks spots along the expected theoretical locations of the ovals to represent the observed stochastic patchiness. The emission pattern of each individual spot is assumed to be of the form $\propto \exp(-(d/H_{\text{spot}})^2)$, where d is the distance from the center of the spot measured in pixel and $H_{\text{spot}} = 2.5$ pixel is a length scale characterizing the size of a spot. The diameter of Ganymede corresponds to ~70 pixels. The radius of Ganymede is $R_G = 2631$ km. Thus, each pixel spans ~75 km on the surface of Ganymede without considerations of projection effects. The spot size when mapped to the regions where the Galileo spacecraft passed the OCFB is roughly comparable to the size of the large magnetic field substructures in this area and is on the same order as the size of the flux transfer events associated with auroral emissions as discussed by *Jia et al.* [2010] for the G8 flyby. We assume that the spots do not exactly lie on the theoretically expected auroral line but that they follow a Gaussian distribution around the expected oval line with a standard deviation of 4 pixels. The associated width mapped to the regions where Galileo spacecraft flybys crossed the OCFB approximately corresponds to a width of 2000 km. Over such length scales Galileo measured highly disturbed spiky magnetic field fluctuations likely associated with flux transfer events or electric current filaments connecting to Ganymede's ionosphere. The number of randomly chosen spots along each oval is approximately 30 in our simulation. This number is consistent with a recurrence rate of flux transfer events [*Jia et al.*, 2010] of 30 s, which when translated to a spatial scale would correspond to 600 km with an assumed spacecraft velocity of 20 km s^{-1}. Assuming a roughly estimated azimuthal length of the upstream magnetopause of 1/2 ($2\pi R_G$), the recurrence scale would lead to approximately 30 flux transfer events. With these values the resultant synthetic images resemble the real observations (e.g., Figure 7). In particular, the resultant average width of the ovals and resultant uncertainty of the rocking angle σ_α are quantitatively similar to the real observations. The distribution functions of the averaged uncertainty $\bar{\sigma}(j_s)$ calculated from 2048 repetitions of randomly generated sets of synthetic images have an expectation value $E[\bar{\sigma}] = 6.9°$. This value is consistent with the average observed uncertainty (see Appendix B) of $\bar{\alpha} \pm 6.3°$, which confirms the applicability of the MC test.

Because the observations show a systematic tendency that the Jovian-facing side of Ganymede is brighter than the anti-Jovian side possibly due to the Hall-effect, we multiply the spot brightness by a weighting function of the form $1+(i_x - R_G)/(2R_G)$. We only include spots whose centers lie within the disk of Ganymede. A random background noise is added to the data with an amplitude similar to the observed background.

In the MC tests as well as in some other parts of the analysis we assumed that the orientation of Jupiter's magnetospheric field does not change during an exposure. During approximately 1000 s the orientation of the magnetic field around maximum magnetic latitudes changes by less than 1% compared to its maximum variability assuming a sinusoidal variation. For all exposures with magnetic latitudes larger than 7° the orientation of the magnetic field changes by only ~10% compared to its maximum variability assuming again a sinusoidal variation. Note, however, that near-maximum magnetic latitudes the Jovian background

©2015. American Geophysical Union. All Rights Reserved.

magnetic field even changes less strongly than sinusoidal due to the current sheet effects which results in less variability of the magnetic field [e.g., *Kivelson et al.*, 1999; *Seufert et al.*, 2011].

Acknowledgments

This work is based on observations with the NASA/ESA Hubble Space Telescope obtained at the Space Telescope Science Institute, which is operated by the Association of Universities for Research in Astronomy (AURA) by the Association of Universities for Research in Astronomy, Inc., under NASA contract NAS 5-26555. We thank A. Roman for scheduling the observations. J.S. acknowledges helpful discussion with Matthias Holschneider (Department of Applied Mathematics, University of Potsdam) on the statistical analysis. The work of this study was funded by STScI, DLR, DFG (Program Planetary Magnetism), and NASA. Numerical computations were executed on the CHEOPS-Cluster of the University of Cologne. The HST data used in this work are available on the MAST archive of STScI. The ZEUS-MP code, which was used to run the MHD model, can be downloaded from http://www.netpurgatory.com/zeusmp.html. The insulating boundary method is provided as Fortran 90 routine in the supporting information of *Duling et al.* [2014] on the JGR-SPACE website.

Larry Kepko thanks the reviewers for their assistance in evaluating this paper.

References

Anderson, J. D., E. L. Lau, W. L. Sjogren, G. Schubert, and W. B. Moore (1996), Gravitational constraints on the internal structure of Ganymede, *Nature*, *384*, 541–543.

Bagenal, F., and P. A. Delamere (2011), Flow of mass and energy in the magnetospheres of Jupiter and Saturn, *J. Geophys. Res.*, *116*, A05209, doi:10.1029/2010JA016294.

Bevington, P. R., and D. K. Robinson (2003), *Data Reduction and Error Analysis for the Physical Sciences*, McGraw Hill, New York.

Chané, E., J. Saur, F. M. Neubauer, J. Raeder, and S. Poedts (2012), Observational evidence of Alfvén wings at the Earth, *J. Geophys. Res.*, *117*, A09217, doi:10.1029/2012JA017628.

Christensen, U. R. (2015), Iron snow dynamo models for Ganymede, *Icarus*, *247*, 248–259, doi:10.1016/j.icarus.2014.10.024.

Christensen, U. R., V. Holzwarth, and A. Reiners (2009), Energy flux determines magnetic field strength of planets and stars, *Nature*, *457*, 167–169, doi:10.1038/nature07626.

Connerney, J. E. P., M. H. Acuna, N. F. Ness, and T. Satoh (1998), New models of Jupiter's magnetic field constrained by the Io Flux Tube footprint, *J. Geophys. Res.*, *103*, 11,929–11,939.

Dessler, A. J. (1983), *Physics of the Jovian Magnetosphere*, Cambridge Univ. Press, New York.

Duling, S., J. Saur, and J. Wicht (2014), Consistent boundary conditions at nonconducting surfaces of planetary bodies: Applications in a new Ganymede MHD model, *J. Geophys. Res. Space Physics*, *119*, 4412–4440, doi:10.1002/2013JA019554.

Eviatar, A., D. J. Williams, C. Paranicas, R. W. McEntire, B. H. Mauk, and M. G. Kivelson (2000), Trapped energetic electrons in the magnetosphere of Ganymede, *J. Geophys. Res.*, *105*, 5547–5554, doi:10.1029/1999JA900450.

Eviatar, A., D. F. Strobel, B. C. Wolfven, P. Feldman, M. A. McGrath, and D. J. Williams (2001), Excitation of the Ganymede ultraviolet aurora, *Astrophys. J.*, *555*, 1013–1019.

Feldman, P. D., M. A. McGrath, D. F. Strobel, H. W. Moos, K. D. Retherford, and B. C. Wolven (2000), HST/STIS ultraviolet imaging of polar aurora on Ganymede, *Astrophys. J.*, *555*, 1085–1090.

Frank, L. A., and W. R. Paterson (2000), Return to Io by the Galileo spacecraft: Plasma observations, *J. Geophys. Res.*, *105*(A11), 25,363–25,378.

Garrison, T. (2006), *Essentials of Oceanography*, Brooks Cole, Belmont, Calif.

Gómez-Pérez, N., and J. Wicht (2010), Behavior of planetary dynamos under the influence of external magnetic fields: Application to Mercury and Ganymede, *Icarus*, *209*, 53–62, doi:10.1016/j.icarus.2010.04.006.

Hall, D. T., D. F. Strobel, P. D. Feldman, M. A. McGrath, and H. A. Weaver (1995), Detection of an oxygen atmosphere on Jupiter's moon Europa, *Nature*, *373*(6516), 677–679.

Hall, D. T., P. D. Feldman, M. A. McGrath, and D. F. Strobel (1998), The far-ultraviolet oxygen airglow of Europa and Ganymede, *Astrophys. J.*, *499*(5), 475–481.

Hand, K. P., and C. F. Chyba (2007), Empirical constraints on the salinity of the European ocean and implications for a thin ice shell, *Icarus*, *189*, 424–438.

Hauck, S. A., J. M. Aurnou, and A. J. Dombard (2006), Sulfur's impact on core evolution and magnetic field generation on Ganymede, *J. Geophys. Res.*, *111*, E09008, doi:10.1029/2005JE002557.

Hernandez, S., et al. (2014), *STIS Instrument Handbook, Version 13.0*, STScI, Baltimore, Md.

Hess, S. L. G., B. Bonfond, P. Zarka, and D. Grodent (2011), Model of the Jovian magnetic field topology constrained by the Io auroral emissions, *J. Geophys. Res.*, *116*, A05217, doi:10.1029/2010JA016262.

Hussmann, H., F. Sohl, and T. Spohn (2006), Subsurface oceans and deep interiors of medium-sized outer planet satellites and large trans-neptunian objects, *Icarus*, *185*, 258–273.

Ip, W., and A. Kopp (2002), Resistive MHD simulations of Ganymede's magnetosphere: 2. Birkeland currents and particle energetics, *J. Geophys. Res.*, *107*(A12), 1491, doi:10.1029/2001JA005072.

Ip, W.-H., A. Kopp, and J. Hu (2004), On the star-magnetosphere interaction of close-in exoplanets, *Astrophys. J.*, *602*, L53–L56.

Jia, X., R. Walker, M. Kivelson, K. Khurana, and J. Linker (2008), Three-dimensional MHD simulations of Ganymede's magnetosphere, *J. Geophys. Res.*, *113*, A06212, doi:10.1029/2007JA012748.

Jia, X., R. Walker, M. Kivelson, K. Khurana, and J. Linker (2009), Properties of Ganymede's magnetosphere inferred from improved three-dimensional MHD simulations, *J. Geophys. Res.*, *114*, A09209, doi:10.1029/2009JA014375.

Jia, X., R. J. Walker, M. G. Kivelson, K. K. Khurana, and J. A. Linker (2010), Dynamics of Ganymede's magnetopause: Intermittent reconnection under steady external conditions, *J. Geophys. Res.*, *115*, A12202, doi:10.1029/2010JA015771.

Khurana, K. K. (1997), Euler potential models of Jupiter's magnetospheric field, *J. Geophys. Res.*, *102*, 11,295–11,306.

Kislyakova, K. G., M. Holmström, H. Lammer, P. Odert, and M. L. Khodachenko (2014), Magnetic moment and plasma environment of HD 209458b as determined from Lyα observations, *Science*, *346*, 981–984, doi:10.1126/science.1257829.

Kivelson, M. G., K. K. Khurana, C. T. Russell, R. J. Walker, J. Warnecke, F. V. Coroniti, C. Polanskey, D. J. Southwood, and G. Schubert (1996), Discovery of Ganymede's magnetic field by the Galileo spacecraft, *Nature*, *384*, 537–541.

Kivelson, M. G., J. Warnecke, L. Bennett, S. Joy, K. K. Khurana, J. A. Linker, C. T. Russell, R. J. Walker, and C. Polanskey (1998), Ganymede's magnetosphere: Magnetometer overview, *J. Geophys. Res.*, *103*, 19,963–19,972, doi:10.1029/98JE00227.

Kivelson, M. G., K. K. Khurana, D. J. Stevenson, L. Bennett, S. Joy, C. T. Russell, R. J. Walker, C. Zimmer, and C. Polanskey (1999), Europa and Callisto: Induced or intrinsic fields in a periodically varying plasma environment, *J. Geophys. Res.*, *104*(A3), 4609–4625.

Kivelson, M. G., K. K. Khurana, and M. Volwerk (2002), The permanent and inductive magnetic moments of Ganymede, *Icarus*, *157*, 507–522.

Kivelson, M. G., F. Bagenal, F. M. Neubauer, W. Kurth, C. Paranicas, and J. Saur (2004), Magnetospheric interactions with satellites, in *Jupiter*, edited by F. Bagenal, pp. 513–536, Cambridge Univ. Press, Univ. of Colo., Cambridge.

Kopp, A., and W. Ip (2002), Resistive MHD simulations of Ganymede's magnetosphere: 1. Time variabilities of the magnetic field topology, *J. Geophys. Res.*, *107*(A12), 1490, doi:10.1029/2001JA005071.

Krist, J. E., R. N. Hook, and F. Stoehr (2011), 20 years of Hubble Space Telescope optical modeling using Tiny Tim, in *Society of Photo-Optical Instrumentation Engineers (SPIE) Conference Series*, vol. 8127, edited by M. A. Kahan, pp. 18–19, SPIE, San Diego, Calif., doi:10.1117/12.892762.

Langel, R. A., and R. H. Estes (1982), A geomagnetic field spectrum, *Geophys. Res. Lett.*, *9*, 250–253, doi:10.1029/GL009i004p00250.

©2015. American Geophysical Union. All Rights Reserved.

Levy, E. H. (1979), Planetary dynamo amplification of ambient magnetic fields, in *Proceedings of the Tenth Lunar and Planetary Science Conference*, vol. 3, edited by N. W. Hinners, pp. 2335–2342, Pergamon Press, Inc., New York.
Marconi, M. L. (2007), A kinetic model of Ganymede's atmosphere, *Icarus*, *190*, 155–174, doi:10.1016/j.icarus.2007.02.016.
McGrath, M. A., X. Jia, K. D. Retherford, P. D. Feldman, D. F. Strobel, and J. Saur (2013), Aurora on Ganymede, *J. Geophys. Res. Space Physics*, *118*, 2043–2054, doi:10.1002/jgra.50122.
Neubauer, F. M. (1998), The sub-Alfvénic interaction of the Galilean satellites with the Jovian magnetosphere, *J. Geophys. Res.*, *103*(E9), 19,843–19,866.
Paty, C., and R. Winglee (2004), Multi-fluid simulations of Ganymede's magnetosphere, *Geophys. Res. Lett.*, *31*, L24806, doi:10.1029/2004GL021220.
Paty, C., and R. Winglee (2006), The role of ion cyclotron motion at Ganymde: Magnetic morphology and magnetospheric dynamics, *Geophys. Res. Lett.*, *33*, L10106, doi:10.1029/2005GL025273.
Paty, C., W. Paterson, and R. Winglee (2008), Ion energization in Ganymede's magnetosphere: Using multifluid simulations to interpret ion engergy spectrograms, *J. Geophys. Res.*, *113*, A06211, doi:10.1029/2007JA012848.
Plainaki, C., A. Milillo, S. Massetti, A. Mura, X. Jia, S. Orsini, V. Mangano, E. De Angelis, and R. Rispoli (2015), The H_2O and O_2 exospheres of Ganymede: The result of a complex interaction between the jovian magnetospheric ions and the icy moon, *Icarus*, *245*, 306–319, doi:10.1016/j.icarus.2014.09.018.
Rambaux, N., T. van Hoolst, and Ö. Karatekin (2011), Librational response of Europa, Ganymede, and Callisto with an ocean for a non-Keplerian orbit, *Astron. Astrophys.*, *527*, A118, doi:10.1051/0004-6361/201015304.
Retherford, K. D., H. W. Moos, D. F. Strobel, and B. C. Wolven (2000), Io's equatorial spots: Morphology of neutral UV emissions, *J. Geophys. Res.*, *105*(A12), 27,157–27,165.
Roth, L., J. Saur, K. D. Retherford, D. F. Strobel, and J. R. Spencer (2011), Simulation of Io's auroral emission: Constraints on the atmosphere in eclipse, *Icarus*, *214*, 495–509, doi:10.1016/j.icarus.2011.05.014.
Roth, L., J. Saur, K. D. Retherford, D. F. Strobel, P. D. Feldman, M. A. McGrath, and F. Nimmo (2014), Transient water vapor at Europa's South Pole, *Science*, *343*, 171–174, doi:10.1126/science.1247051.
Saur, J. (2004), A model for Io's local electric field for a combined Alfvénic and unipolar inductor far-field coupling, *J. Geophys. Res.*, *109*, A01210, doi:10.1029/2002JA009354.
Saur, J., D. F. Strobel, and F. M. Neubauer (1998), Interaction of the Jovian magnetosphere with Europa: Constraints on the neutral atmosphere, *J. Geophys. Res.*, *103*(E9), 19,947–19,962.
Saur, J., F. M. Neubauer, D. F. Strobel, and M. E. Summers (2000), Io's ultraviolet aurora: Remote sensing of Io's interaction, *Geophys. Res. Lett.*, *27*(18), 2893–2896.
Saur, J., F. M. Neubauer, and K.-H. Glassmeier (2010), Induced magnetic fields in solar system bodies, *Space Sci. Rev.*, *152*, 391–421, doi:10.1007/s11214-009-9581-y.
Saur, J., et al. (2011), Hubble space telescope/advanced camera for surveys observations of Europa's atmospheric ultraviolet emission at eastern elongation, *Astrophys. J.*, *738*, 153, doi:10.1088/0004-637X/738/2/153.
Saur, J., T. Grambusch, S. Duling, F. M. Neubauer, and S. Simon (2013), Magnetic energy fluxes in sub-Alfvénic planet star and moon planet interactions, *Astron. Astrophys.*, *552*, A119, doi:10.1051/0004-6361/201118179.
Schilling, N., F. M. Neubauer, and J. Saur (2007), Time-varying interaction of Europa with the jovian magnetosphere: Constraints on the conductivity of Europa's subsurface ocean, *Icarus*, *192*, 41–55.
Schilling, N., F. M. Neubauer, and J. Saur (2008), Influence of the internally induced magnetic field on the plasma interaction of Europa, *J. Geophys. Res.*, *113*, A03203, doi:10.1029/2007JA012842.
Seufert, M., J. Saur, and F. M. Neubauer (2011), Multi-frequency electromagnetic sounding of the Galilean moons, *Icarus*, *214*, 477–494, doi:10.1016/j.icarus.2011.03.017.
Sohl, F., T. Spohn, D. Breuer, and K. Nagel (2002), Implications from Galileo observations on the interior structure and chemistry of the Galilean satellites, *Icarus*, *157*, 104–119.
Telford, W. M. (1993), *Applied Geophysics*, Cambridge Univ. Press, Cambridge, New York.
Vance, S., M. Bouffard, M. Choukroun, and C. Sotin (2014), Ganymede's internal structure including thermodynamics of magnesium sulfate oceans in contact with ice, *Planet. Space Sci.*, *96*, 62–70, doi:10.1016/j.pss.2014.03.011.
Volwerk, M., M. G. Kivelson, K. K. Khurana, and R. L. McPherron (1999), Probing Ganymede's magnetosphere with field line resonances, *J. Geophys. Res.*, *104*(A7), 14,729–14,738.
Williams, Q. (2009), Bottom-up versus top-down solidification of the cores of small solar system bodies: Constraints on paradoxical cores, *Earth Planet. Sci. Lett.*, *284*, 564–569, doi:10.1016/j.epsl.2009.05.019.
Woods, T. N., F. G. Eparvier, S. M. Bailey, P. C. Chamberlin, J. Lean, G. J. Rottman, S. C. Solomon, W. K. Tobiska, and D. L. Woodraska (2005), Solar EUV Experiment (SEE): Mission overview and first results, *J. Geophys. Res.*, *110*, A01312, doi:10.1029/2004JA010765.
Zimmer, C., K. Khurana, and M. Kivelson (2000), Subsurface oceans on Europa and Callisto: Constraints from Galileo magnetometer observations, *Icarus*, *147*, 329–347.

©2015. American Geophysical Union. All Rights Reserved.